Research Square

Preprints are preliminary reports that have not undergone peer review.
They should not be considered conclusive, used to inform clinical practice,
or referenced by the media as validated information.

Influence of Mg doping on the structural, magnetic, optical, and electrical properties of Co–Zn spinel ferrites

Samyuktha B. S
Sri Sai Ram Engineering College
Sathiya Priya A
priyasathiya8@gmail.com

Sri Sai Ram Engineering College
Jayalakshmi D. S
Sathyabama Institute of Science and Technology (Deemed to be University)

Research Article

Keywords: Mg doped Co-Zn ferrite, sol-gel method, Elastic modulus, Nyquist plot, SFD

Posted Date: November 11th, 2026

DOI: https://doi.org/10.21203/rs.3.rs-11234661/v1

License: This work is licensed under a Creative Commons Attribution 4.0 International License.
Read Full License

Additional Declarations: No competing interests reported.

Influence of Mg doping on the structural, magnetic, optical, and electrical properties of Co–Zn spinel ferrites

B. S. Samyuktha[a], A. Sathiya Priya[a]*, D.S. Jayalakshmi[b]

[a]Department of Physics, Sri Sai Ram Engineering College, Chennai, Tamil Nadu, India

[b]Department of Physics, Sathyabama Institute of Science and Technology (Deemed to be University), Chennai, Tamil Nadu, India

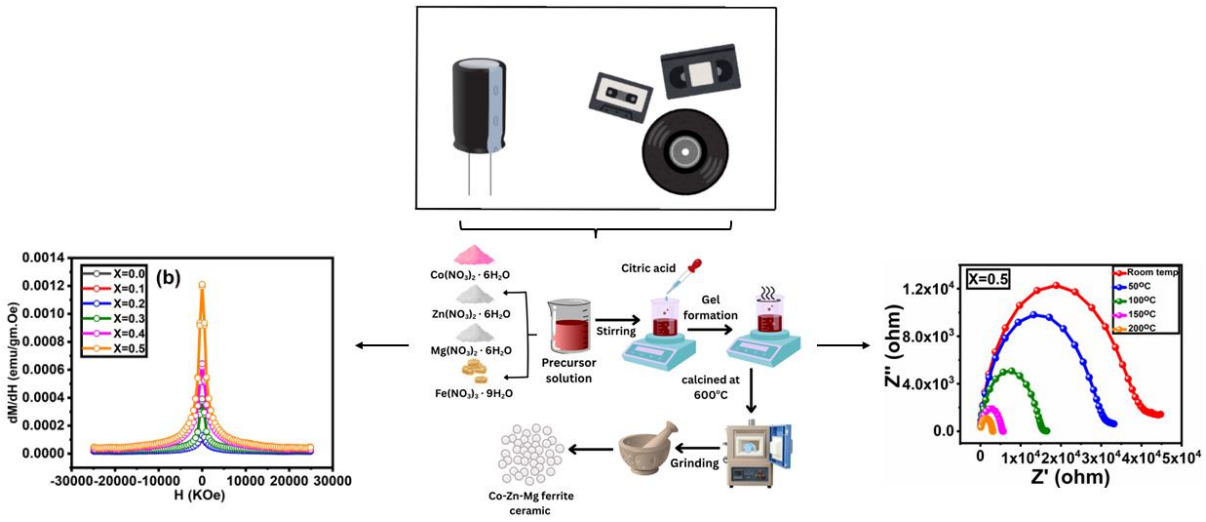
*Corresponding author: priyasathiya8@gmail.com

Abstract

The effect of Mg substitution on the structural, vibrational, optical, magnetic, dielectric, and electrical properties of cobalt–zinc ferrite was systematically investigated using $Co_{0.5}Zn_{0.5-x}Mg_xFe_2O_4$ (x = 0.0–0.5) ceramics synthesized by the sol–gel method. X-ray diffraction and Rietveld refinement confirmed the formation of a single-phase cubic spinel structure (space group $Fd\bar{3}m$) for all compositions. Structural parameters, including cation–cation and cation–anion distances, were systematically analyzed, revealing crystallite sizes in the range of 13.47–25.92 nm. FTIR spectra exhibited characteristic absorption bands near 650 and 460 cm^{-1}, corresponding to tetrahedral and octahedral metal–oxygen vibrations, accompanied by slight reductions in bond length, force constant, and Debye temperature. Optical analysis revealed a gradual decrease in the band gap from 1.72 to 1.43 eV with increasing Mg content, indicating modifications in the electronic structure. Magnetic measurements confirmed ferromagnetic behavior with a multidomain nature, while a single-peak switching field distribution indicated uniform magnetization reversal. The $Co_{0.5}Zn_{0.5}Mg_{0.5}Fe_2O_4$ composition exhibited the highest saturation magnetization among all Mg-substituted samples. Dielectric studies demonstrated that this composition possessed a high dielectric constant with comparatively low dielectric loss. Impedance and modulus analyses revealed non-Debye relaxation behavior, whereas Nyquist plots confirmed the contributions of both grains and grain boundaries to the electrical conduction process. These findings demonstrate that Mg substitution effectively tailors the multifunctional properties of Co–Zn ferrites, making $Co_{0.5}Zn_{0.5}Mg_{0.5}Fe_2O_4$ a promising material for high-frequency electronic and memory device applications.

Keywords: Mg doped Co-Zn ferrite, sol-gel method, Elastic modulus, Nyquist plot, SFD.

Graphical abstract



1. Introduction

The rapid advancedment of electronic technologies and the growing demand for sustainable energy solutions have created an increasing need for advanced materials that deliver enhanced performance, high reliability and improved energy efficiency. As electronic devices continue to become smaller, faster, and more energy efficient, they require materials that can support high-speed operations while minimizing power consumption. At the same time, reducing energy losses during device operation has become a critical requirement for improving overall device efficiency. Furthermore, the increasing use of renewable energy sources and smart electronics has highlighted the importance of materials with excellent optical, dielectric and magnetic properties for next generation energy efficient electronic applications. Among various functional materials, spinel ferrites have attracted considerable attention due to their combinations of high electrical resistivity, low eddy current loss, tunable magnetic properties, and excellent chemical stability making them promising candiates for high frquency electronic devices, sensors, energy storage systems and spintronics applications [1, 2].

Ferrites generally possess the chemical formula AB_2O_4, where the A-site cations occupy tetrahedral sites and the B-site cations occupy octahedral sites within the spinel crystal structure. However, the distribution of cations is not always fixed, and many ferrites exhibit normal, inverse, or mixed spinel structures, in which cations are distributed between the tetrahedral and octahedral sites depending on their ionic size, valence state, and synthesis conditions [3]. Such cation redistribution plays a crucial role in determining the structural, electrical, dielectric, and magnetic properties of spinel ferrites, thereby enabling their application in a wide range of advanced electronic and magnetic devices. Among the various

spinel ferrites, cobalt–zinc (Co–Zn) ferrites have attracted considerable attention owing to their tunable magnetic properties, excellent chemical stability, and favorable electrical characteristics. Co–Zn ferrites crystallize in a cubic spinel structure and can be represented by the cation distribution $(Zn^{2+}_{1-x}Fe^{3+}_{1-x})[Co^{2+}_{x}Fe^{3+}_{1+x}]O_4$, where the parentheses denote tetrahedral (A) sites and the square brackets represent octahedral (B) sites [4]. Despite these advantages, pure Co–Zn ferrites exhibit certain limitations, including moderate magnetic response, relatively high dielectric loss, and limited control over their electrical transport properties, which restrict their performance in advanced electronic applications. Consequently, partial substitution with suitable divalent cations has become an effective strategy for tailoring their functional properties.

Among the various dopant ions investigated, Mg^{2+} has emerged as an attractive substituent because of its non-magnetic nature, suitable ionic radius, chemical stability, and ability to modify the cation distribution within the spinel lattice. In $Co_{0.5}Zn_{0.5-x}Mg_xFe_2O_4$ ferrites, both Zn^{2+} and Mg^{2+} preferentially occupy the tetrahedral (A) sites, whereas Co^{2+} ions predominantly occupy the octahedral (B) sites, while Fe^{3+} ions are distributed over both sublattices to maintain charge neutrality and structural stability. The substitution of Mg^{2+} for Zn^{2+} induces subtle lattice distortions and modifies the defect chemistry and cation distribution, thereby influencing the Fe^{2+}/Fe^{3+} hopping mechanism responsible for electrical conduction. Furthermore, the relatively smaller ionic radius of Mg^{2+} suppresses excessive grain growth during sintering, resulting in a refined microstructure with increased grain-boundary resistance. These microstructural modifications significantly influence polarization behavior, charge carrier mobility, dielectric relaxation, and electrical conductivity [5, 6]. Magnetically, the properties of spinel ferrites are governed by superexchange interactions between magnetic ions through oxygen anions, where the dominant A–B interaction produces antiparallel spin alignment between the tetrahedral and octahedral sublattices. Consequently, the net magnetization arises from the difference between the magnetic moments of the two sublattices [7, 8]. Owing to their high electrical resistivity, low dielectric loss, moderate saturation magnetization, and strong magnetocrystalline anisotropy, Mg-substituted Co–Zn ferrites are considered promising materials for high-frequency electronic components, magnetic recording media, sensors, and energy storage applications. In addition to chemical composition, the synthesis method plays a vital role in determining the structural and functional properties of ferrite ceramics by influencing particle size, phase purity, crystallinity, grain morphology, and cation distribution. Among the various synthesis

techniques, the sol–gel method has attracted significant attention because it provides excellent compositional homogeneity, precise control over stoichiometry, relatively low processing temperatures, and uniform grain growth, resulting in highly crystalline ferrite ceramics with improved electrical and magnetic properties [9]. Several researchers have successfully employed this method to tailor the properties of Co–Zn-based ferrites. For example, Badiger et al. [10] investigated Cr-substituted Co–Zn ferrites prepared by a self-ignited sol–gel method and reported enhanced dielectric and magnetic properties. Sayed et al. [11] synthesized Zn-substituted Co–Ni ferrites using the sol–gel auto-combustion technique and observed a decrease in the dielectric constant with increasing Zn^{2+} concentration. Similarly, Thammarong et al. [12] demonstrated that Ca substitution improved the magnetic properties of Co–Zn ferrites through modifications in cation distribution, whereas Mn-substituted Co–Zn ferrites prepared by the co-precipitation method exhibited enhanced AC resistivity with increasing dopant concentration [13]. Although several studies have reported the structural, magnetic, and electrical properties of Mg-substituted Co–Zn ferrites at room temperature [7, 14-16], systematic investigations of the temperature-dependent dielectric relaxation, impedance spectroscopy, electric modulus, AC conductivity, activation energy, and Bode analysis of $Co_{0.5}Zn_{0.5-x}Mg_xFe_2O_4$ ceramics synthesized by the sol–gel route remain scarce. Therefore, the present work investigates the influence of Mg^{2+} substitution on the structural, dielectric, optical, and relaxation characteristics of $Co_{0.5}Zn_{0.5-x}Mg_xFe_2O_4$ (x = 0.0–0.5) ferrite ceramics synthesized by the sol–gel method. Particular emphasis is placed on understanding the effect of Mg incorporation on the temperature-dependent dielectric behavior, impedance response, electric modulus, AC conductivity, activation energy, and Bode characteristics. The use of Mg^{2+} as a non-toxic and environmentally benign dopant provides an effective route for tailoring the multifunctional properties of Co–Zn ferrites, thereby expanding their potential for high-frequency electronics, magnetic recording systems, and energy-related device applications.

2. Experimental details

$Co_{0.5}Zn_{0.5-x}Mg_xFe_2O_4$ (x = 0.0–0.5) ceramics were synthesized by the sol–gel method, as presented in Fig. S1. Cobalt nitrate (Sigma-Aldrich, 99%), zinc acetate (Sigma-Aldrich, 98%), magnesium nitrate (Sigma-Aldrich, 99%), and ferric nitrate (Sigma-Aldrich, 98%) were used as precursor materials without further purification. Appropriate stoichiometric amounts of the precursors were accurately weighed and dissolved in double-deionized water to obtain a clear and homogeneous solution. Citric acid (Sigma-Aldrich, 99%) was used as

the complexing agent, maintaining a 1:1 molar ratio with the total metal-ion concentration. The resulting solution was continuously stirred at approximately 70 °C for 5 h, leading to the formation of a viscous sol. As the water gradually evaporated and metal ions formed complexes with citric acid, the sol transformed into a uniform brown gel. The gel was subsequently dried to obtain a dark brown precursor powder, which was calcined in air at 600 °C for 3 h in a muffle furnace. After cooling to room temperature, the calcined product was ground using an agate mortar and pestle and used for further characterization. Hereafter, the ferrites $Co_{0.5}Zn_{0.5}Fe_2O_4$, $Co_{0.5}Zn_{0.4}Mg_{0.1}Fe_2O_4$, $Co_{0.5}Zn_{0.3}Mg_{0.2}Fe_2O_4$, $Co_{0.5}Zn_{0.2}Mg_{0.3}Fe_2O_4$, $Co_{0.5}Zn_{0.1}Mg_{0.4}Fe_2O_4$, and $Co_{0.5}Mg_{0.5}Fe_2O_4$ are denoted as x = 0.0, 0.1, 0.2, 0.3, 0.4, and 0.5, respectively.

2.1. Measurement techniques

The crystal structure of $Co_{0.5}Zn_{0.5-x}Mg_xFe_2O_4$ (x = 0.0–0.5) ceramics was examined by X-ray diffraction (XRD) using a PANalytical X'Pert Powder diffractometer with Cu Kα radiation (λ = 1.5406 Å). The lattice parameters were calculated using UnitCellWin software. Rietveld refinement was performed using the FullProf Suite to confirm the phase purity of the synthesized ceramics, while phase identification was carried out using X'Pert HighScore software (version 3.0). Fourier transform infrared (FTIR) spectra were recorded using an IRAffinity-1 (Shimadzu)/Nicolet iS50 spectrometer in the range of 4000–400 cm^{-1} to confirm the presence of metal–oxygen bonds. Diffuse reflectance spectroscopy (DRS) measurements were performed using a LABINDIA UV-3092 spectrophotometer to determine the optical band gap of the synthesized ceramics. The magnetic properties were investigated using a Lake Shore 7404 vibrating sample magnetometer (VSM) (Lake Shore, Westerville, OH, USA). The electrical and dielectric properties of the sintered ceramic pellets were measured using a dielectric impedance analyzer over the frequency range of 1 Hz–7 MHz. Prior to the measurements, both surfaces of the sintered pellets were coated with conducting silver paste to ensure good electrical conductivity and reliable electrical contact.

3. Result and discussion

3.1. Structural properties

The XRD analysis of $Co_{0.5}Zn_{0.5-x}Mg_xFe_2O_4$ where (x= 0.0–0.5) are presented in Fig. 1(a). The peaks are indexed to (111), (220), (311), (400), (511), and (531) these planes confirm the formation of a spinel cubic crystal structure [17]. Peaks align closely with the cubic spinel phase (JCPDS card no. 00-022-1012), confirming purity of phase and Phase identification were performed using X'Pert HighScore software (version 3.0). All compostions exhibit a

face-centered cubic lattice with the *Fd3m* space group. For the undoped sample (x = 0.0), weak additional diffraction peaks, marked by * and #, were identified as the Co_3O_4 and Fe_2O_3 secondary phases, respectively. As the concentration of Mg^{2+} increases, these impurity phases gradually disappear, suggesting that Mg^{2+} incorporation encourages phase stabilization and noticeable peak broadening. The inset Fig. 1(b), which magnifies the (311) peak, clearly demonstrates a gradual sharpening of the peak with Mg^{2+} incorporation. Addionally, The (311) peak for x = 0.0–0.2 ceramics shifts slightly toward lower diffraction angles, induced cation redistribution leads to an expansion of the lattice. In contrast, the sample x =0.3 – 0.5 exhibits a marginal shift toward higher angles, suggesting a slight contraction of the lattice. This can be attributed to the influenc of Mg^{2+} in local lattice disortion, increased interionic interactions and reduced lattice spacing. Moreover, this shift can be linked to the substitution of larger Zn^{2+} (0.74 Å) by relatively small Mg^{2+} (0.65 Å), which alters the lattice constant. In addition, the introduction of Mg incorporation also influences lattice constant values in a prepared ceramics which initially decreases with increasing in Mg content and then shows an increasing trend at higher concentration. This non-linear variation does not obey Vegard's law. [16]. At lower Mg content, Mg^{2+} species occupy the position of Zn^{2+} species at the tetrahedral (A) position due to their similar valence and coordination. As the Mg content increases, partial redistribution of cations occurs, where Mg^{2+} ions can also occupy octahedrally (B) coordination, accompanied by the redistribution of Fe^{3+} species from octahedrally to tetrahedrally sites to maintain structural stability [18]. Similar non-linear angle shifting and non-monotonic variation of lattice parameters for have been reported earlier for $Zn_xCo_{1-x}Fe_2O_4$ [19], $Zn_{0.4}Co_{0.6-x}Mg_xFe_{1.9}La_{0.1}O_4$ [20].

The lattice constant values and cell volume of Mg doped Co-Zn ferrites were calculated values are noted in Table1 and then variations are depicted in Fig. S2(a). The similar trend in cell volume attributed to lattice expansion at higher Mg contents may result from cation redistribution between tetrahedrally and octahedrally coordination sublattices, and increased occupancy of Mg^{2+} and Fe^{3+} in B sites, which is greater influence on lattice dimensions because of different ionic radii and site preferences [16].

The lattice microstrain (ε) was calculated using the Williamson–Hall (W–H) plot, which separates the contributions of crystallite size and lattice strain to the X-ray diffraction peak broadening. The calculated crystal size and microstrain values all prepared ceramics are listed in Table 1. The crystallite size of all the ceramics shows a non-linear variation with Mg substitution. The x=0.0 sample shows the largest crystallite size (25.92 nm). With initial Mg

substitution x=0.1 and x=0.2, the crystallite size drops sharply to 13.93 and 13.47 nm respectively, due to lattice distortion and enhanced nucleation caused by Mg^{2+} ions. At higher Mg contents ($x \geq 0.3$), the crystallite size increases steadily, reaching 19.88 nm at x=0.5 indicating improved lattice stability and crystallinity, where reduced strain and better cation ordering favor grain growth during sintering. Similarly, Beyranvand et al. [21] reported a similar non-monotonic variation in crystallite size for $Mn_{0.3-x}Cd_xCu_{0.2}Zn_{0.5}Fe_2O_4$ synthesized via the citrate–nitrate method, while Zhang et al.[22] observed comparable behavior in Mn doped Ni–Co ferrites synthesized by the autocombustion method. In the W–H plot, slope of the fitted line reflects the nature of the lattice strain. The positive slopes observed in the W–H plots (Fig. S3) indicate the presence of tensile strain in all preapared samples may be contributes to observed lattice expansion.

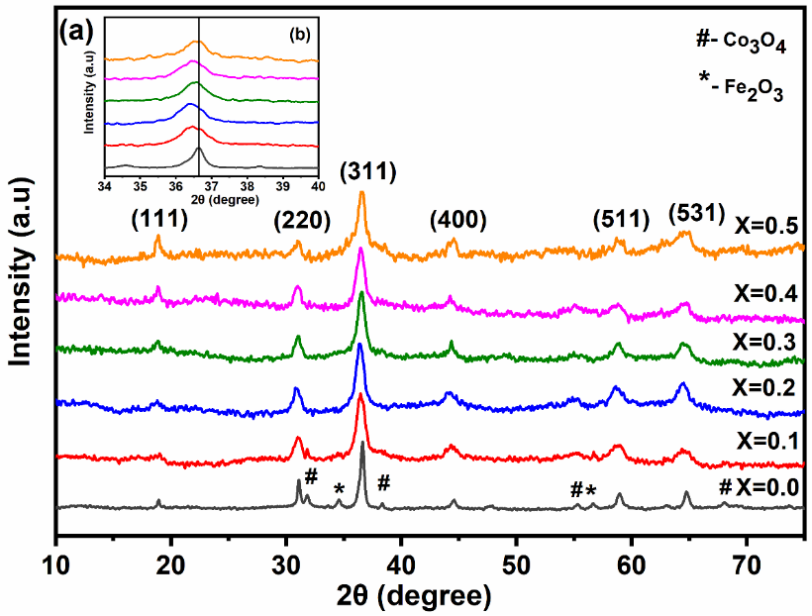


Fig. 1. **(a)** XRD pattern of $Co_{0.5}Zn_{0.5-x}Mg_xFe_2O_4$ ($x = 0.0 – 0.5$) **(b)** Enlarged peak at the plane (311).

Dislocation density (δ), surface-to-volume ratio (S/V), and X-ray density (ρ_x) are important microstructural parameters that provide valuable insights into the crystalline defect structure, particle geometry, and packing characteristics of the synthesized ceramics. These parameters were calculated using the standard equations and the obtained values are presented in Table 1. An initial increase in dislocation density is observed with Mg incorporation samples due to structural distortion and strain generation by Mg substitution. At higher dopent concentration, the dislocation density decreases indicating strain relaxation and lower dislocation densities are more crystalline [23]. As presented in Table 1, when crystal size is larger are associated with lower number of dislocations, confirming that crystallite

growth leads to improved lattice ordering and enhanced crystallinity. The surface/volume ratio shows an increases at lower Mg concentration, consistent with the corresponding decreases in crystallite size. At x=0.3 sample, the S/V ratio decreases, reflects enhanced grain growth and reduced surface defect density. This inverse relationship between crystallite size and S/V ratio further confirms the microstructural evolution induced by Mg^{2+} incorporation.

The X-ray density (ρ_x), calculated from the crystallographic parameters, reflects the changes in crystal structure dimensions and atomic packing induced by the incorporation of small amounts of dopant. The observed non-linear variation in ρ_x as summarized in Table 1. Higher Mg substitution, the substitution of Zn^{2+} by Mg^{2+} along with lattice expansion at higher Mg contents and also difference in ionic radii and structural disortion may cause to lattice constant increases, resulting in a reduction in density. A similar values was reported for Mg-substituted Zn-Co-Fe-La nano ferrite by Arshad et al. [20], with values in the range of 5.0 to 5.48 g/cm^3.

Table 1

Structural parameters of synthesized $Co_{0.5}Zn_{0.5-x}Mg_xFe_2O_4$ (X=0.0 – 0.5).

Sample code/ Parameters	**x = 0.0**	**x = 0.1**	**x = 0.2**	**x = 0.3**	**x = 0.4**	**x = 0.5**
Lattice constant *a* (Å)	8.3052	8.3049	8.2985	8.3158	8.3214	8.3266
Crystal size *D* (nm)	25.92	13.93	13.47	14.74	16.23	19.88
Unit Cell Volume *V* (Å)^3	572.86	572.80	571.48	575.07	576.24	577.31
Microstrain (ε) ($\times10^{-2}$)	1.535	3.933	4.186	3.374	3.296	3.244
Lattice Strain using W-H method (ε) ($\times10^{-3}$)	3.28	8.37	9.56	5.21	4.60	1.84
Dislocation density δ ($\times10^{-3}$ /m^2)	1.4884	5.1608	5.5114	4.6026	3.7963	2.5302
S/V (Å)$^{-1}$	0.7224	0.7224	0.7230	0.7215	0.7210	0.7205
X-Ray density ρ_x (g/cm^3)	5.32	5.42	5.52	5.21	5.10	5.00
Specific surface area S (m^2/g)	43.51	79.46	80.69	78.12	72.48	60.36
Packing factor P	119.32	51.21	49.27	54.10	59.62	73.14

Ionic radius	r_A **(Å)**	0.56443	0.56438	0.56293	0.56686	0.56813	0.56930
	r_B **(Å)**	0.70646	0.70640	0.70484	0.70907	0.71044	0.71170
Tolerance factor (*t*)		0.99747	0.99749	0.99783	0.99688	0.99690	0.99608

The calculated specific surface area (S) and packing factor (p) values are summarized in Table 1. The specific surface area increased from 43.51 $m^2\ g^{-1}$ for the undoped sample to a maximum of 80.69 $m^2\ g^{-1}$ at x = 0.2. This can be linked to reduction in crystallite size and creation of more surface-active sites. With further rising in composition, the surface area gradually decreases to 60.36 $m^2\ g^{-1}$ (x = 0.5), related to an increases crystal size and particle agglomeration. Also, packing factor initially decreases from 119.32 to 49.27 up to x = 0.2, indicating increased structural looseness, and then increases again to 73.14 at higher concentration, suggesting improved packing density. A comparable trend was reported for Mg-substituted Zn–Co–Fe–La nanoferites by Arshad et al. [20] supporting the observed structural behavior. The inverse variation between S and P indicates that the x=0.2 substituion show maximum surface availability and structural porosity.

The average ionic radii of tetrahedrally (r_A) and octahedrally radii (r_B) were evaluated by Standley's relation [15]:

$$r_A = (u - 0.25)a\sqrt{3} - R_0 \qquad (1)$$

$$r_B = (0.625 - u)a - R_0 \qquad (2)$$

Where u represents the oxygen positional value (u = 0.381), R_0 denotes radius of the oxygen ion, a denotes lattice parameter. The calculated tetrahedral (r_A) and octahedral (r_B) ionic radii for Co-Zn Ferrite and Mg doped Co-Zn Ferrite samples shows in Fig. S2(b) and table 1, a slight reduction from x=0.0 to x=0.2 ceramics rising Mg concentration, related to incorporation of Mg^{2+} (0.65 Å) in Zn^{2+} (0.74 Å), primarily at A site. For higher concentration from x=0.3 to x=0.5 sample, gradual rise in both r_A and r_B is observed. This process shows the redistribution of cations from A to B positions, where Mg^{2+} ions increasingly occupy both sites and are accompanied by Fe^{3+} migration to maintain charge neutrality and structural stability [24]. To understand the charge transport behavior, the hopping lengths between neighbouring cations at tetrahedrally (d_A) and octahedrally (d_B) positions and corresponding

bond lengths, shared and unshared edge parameters of both sites, were calculated by using below relations [25]:

$$\left.\begin{aligned} d_A &= 0.25\, a\sqrt{3}\,;\; d_B = 0.25\, a\,\sqrt{2} \\ d_{A\times} &= a\sqrt{3}\left(u - \frac{1}{4}\right) \\ d_{B\times} &= a\sqrt{\left[3u^2 - \left(\frac{11}{4}\right)u + \frac{43}{64}\right]} \\ d_{A\times E} &= a\sqrt{2}\left(2u - \frac{1}{2}\right) \\ d_{B\times E} &= a\sqrt{2}(1-2u) \\ d_{B\times EU} &= a\sqrt{4u^2 - 3u + \left(\frac{11}{16}\right)} \end{aligned}\right\} \quad (3)$$

These parameters are shown in Table 2. All calculated distances shows slight decrease, followed by a gradual increase with further Mg substitution in both tetrahedrally and octahedrally sublattices. The tetrahedrally coordination bond length (d_A) exhibit slight reduction from 3.59625 Å at x=0.0 to 3.59338 Å at x=0.2, a gradual rise with further Mg substitution. A same series is seen for the B-site (d_B). A parameters $d_{A\times}$ and $d_{B\times}$ representing effective nearest-neighbor separations and edge and face-shared octahedral distances ($d_{A\times E}$, $d_{B\times E}$, and $d_{B\times EU}$) also exhibit a non-monotonic variation with Mg substitution. The initial reduction in all parameters at lower concentration is attributed to the incorporation of smaller Mg^{2+} in larger Zn^{2+}, resulting local distortion. This is corresponding to observed decrease in lattice constant and increased microstrain observed from Williamson–Hall analysis at intermediate Mg^{2+} levels. Beyond x=0.2 samples, the rise in both A–O and B–O bond lengths indicates lattice expansion, which is caused by cation redistribution between tetrahedrally and octahedrally coordiantion, accompanied by Fe^{3+} migration to maintain structural stability. It is evident that d_A is consistently larger than d_B across all samples, showing that cations are more closely spaced in octahedrally position than tetrahedrally position under ambient conditions [25]. A calculated values are increases because of size of the grain increases, as grain growth significantly influences structural responses. A parallel trend was seen by Masuku et al. [26], Gd^{3+} substitution in Zn–Ni ferrites prepared through glycol thermal route, and by Abu Elsaad et al. [27] for Erbium doped Mn–Cu ferrites prepared using the auto-combustion method. Finally, a low level of Mg substitution influences structural characteristic of Mg doped Co-Zn ferrite.

Table 2

Structural distance and edge parametes for $Co_{0.5}Zn_{0.5-x}Mg_xFe_2O_4$ (x = 0.0 – 0.5).

Sample code/ parameters	d_A **(Å)**	d_B **(Å)**	$d_{A\times}$ **(Å)**	$d_{B\times}$ **(Å)**	$d_{A\times E}$ **(Å)**	$d_{B\times E}$ **(Å)**	$d_{B\times EU}$ **(Å)**
x = 0.0	3.59625	2.93398	1.88443	2.02613	3.07727	2.79538	2.93796
x = 0.1	3.59614	2.93624	1.88438	2.02607	3.07718	2.79530	2.93787
x = 0.2	3.59338	2.93398	1.88293	2.02451	3.07481	2.79315	2.93561
x = 0.3	3.60088	2.94010	1.88686	2.02874	3.08123	2.79898	2.94174
x = 0.4	3.60331	2.94209	1.88813	2.03011	3.08331	2.80087	2.94372
x = 0.5	3.60554	2.94391	1.88930	2.03136	3.08521	2.80260	2.94554

In tolerance factor, lattice distortion in spinel structures arises from variations in ionic radii and cation occupancy over tetrahedrally and octahedrally coordination position, and this distortion can be effectively analyzed for the Co-Zn ferrites and Mg doped Co-Zn ferrites spinel structure are using the following relation,

$$t = \frac{1}{\sqrt{3}}\left(\frac{r_A + R_o}{r_B + R_O}\right) + \frac{1}{\sqrt{2}}\left(\frac{R_o}{r_B + R_O}\right) \qquad (4)$$

Table 1 summarizes the (*t*) values. The tolerance factor values remain unity, confirming the stability of the cubic phase for all samples. A slight rise in (*t*) up to x=0.2 sample, while the subsequent decrease at higher Mg concentration. The occurance of Zn^{2+} cations in the tetrahedrally (A) coordination leads to local lattice distortion and relaxation effects in the spinel framework is responsible for this behavior.

The parametes are used to determine the distance associated with metal-oxygen and metal-metal ionic pairs by using the following equation and parameters, noted in table 3.

$$p = a\left(\frac{5}{8} - u\right) \;\&\; q = a\sqrt{3}\left(u - \frac{1}{4}\right)$$

$$r = a\sqrt{11}\left(u - \frac{1}{4}\right) \;\&\; s = a\sqrt{3}\left(\frac{u}{3} + \frac{1}{8}\right)$$

$$\left.\begin{aligned} b = \sqrt{2}\left(\frac{a}{4}\right) \;\&\; c = \sqrt{11}\left(\frac{a}{8}\right) \\ d = \sqrt{3}\left(\frac{a}{4}\right) \;\&\; e = \sqrt{3}\left(\frac{3a}{8}\right) \\ f = \sqrt{6}\left(\frac{a}{4}\right) \end{aligned}\right\} \quad (5)$$

At lower values of Mg^{2+} concentration (x = 0.1 and 0.2) decrease of interionic distances is seen, indicating a local lattice contraction. This behavior is associated with cation redistribution linking A and B positions, where Mg^{2+} ions tend to reside octahedrally position, pushing Fe^{3+} ions out of B site. This redistribution changes the geometry of Fe–O–Fe bond, and so make the superexchange interactions stronger at short ranges. As Mg contents (x ≥ 0.3) increases, a gradual increase in all interionic distances. This expansion is mainly because larger ionic radius of Mg^{2+} and the weakening of Fe–O bonds, which increases bond lengths and reduces orbital overlap. These modification have a straight affect on magnetic behavior. The increase in interionic distances reduces A–B superexchange interactions, which are sensitive to bond length. As a result, Mg content rises, magnetization decrease because of magnetic dilusion Fe^{3+}–O–Fe^{3+} linkages by non-magnetic Mg^{2+} ions. This also contributes to enhanced magnetic softness due to decrease in coercive field of the ferrite systems.

Table 3

Calculated value of cation-cation and cation-anion distance of $Co_{0.5}Zn_{0.5-x}Mg_xFe_2O_4$ (X=0.0 – 0.5).

Sample code/ Parameters	**x = 0.0**	**x = 0.1**	**x = 0.2**	**x = 0.3**	**x = 0.4**	**x = 0.5**
p	2.02646	2.02640	2.02484	2.02907	2.03044	2.03170
q	1.88443	1.88438	1.88293	1.88686	1.88813	1.88930
r	3.60842	3.60831	3.60554	3.61306	3.61550	3.61774
s	3.62502	3.62491	3.62212	3.62968	3.63213	3.63438
b	2.93633	2.93624	2.93398	2.94010	2.94209	2.94391
c	3.44315	3.19484	3.44040	3.44758	3.44990	3.45204
d	3.59625	3.59614	3.59338	3.60088	3.60331	3.60554
e	5.39264	5.39422	5.39007	5.40132	5.40496	5.40831
f	5.08587	5.08572	5.08180	5.09241	5.09585	5.09900

3.1.1. Rietveld refinement analysis

Fig. 2 presents the Rietveld-refined XRD patterns of spinel Mg-doped Co–Zn–Fe ceramics. In the Fig. 2, closely matches the observed and calculated diffraction patterns, along with proper alignment of the Bragg reflections and minimal residual differences, confirms the formation of a cubic spinel phase with a single phase nature for all incorporation (x = 0.1–0.5) with the space group (*Fd3m*). The low chi-square (χ^2) values for all samples (1.37 - 1.61) confirm that the fitted parameters are good and the fits are of good quality. The refined lattice constant was found to vary with Mg substitution. The lattice constant initially increased (8.1676 Å) for x = 0.1 to (8.2213 Å) for x = 0.2, followed by a slight reduction at x = 0.3 and then rises again for higher Mg concentrations. A similar trend was observed for the unit cell volume. These variation can be associate with the substitution of Mg^{2+} in place of Zn^{2+} may also introduce slight structural distortions because of vary in ionic radius, leading to minor changes in the structural characteristics derived from refinement [27]. Slight variation observed in intensities may be related to the creation of lattice defects, cation redistribution within the spinel lattice. At the same time, variations in defect concentration and dislocation density can influence the lattice constant and interatomic bond lengths [17]. Density value slightly decreased as Mg content rises related to the alteration of crystal packing. The structural parameters from refinements of each composition are listed in Table S1. For instance, Akhtar et al. [17] given χ^2 value approximately 1.03–1.81 for Co-doped MgZn spinel nanoferrites prepared by the sol–gel ignited method. The close similarity between the present χ^2 values and those reported in earlier studies validate the good quality of refinement, suggests that synthesized $Co_{0.5}Zn_{0.5-x}Mg_xFe_2O_4$ samples possess good crystallinity possessing a cubic spinel crystal lattice.

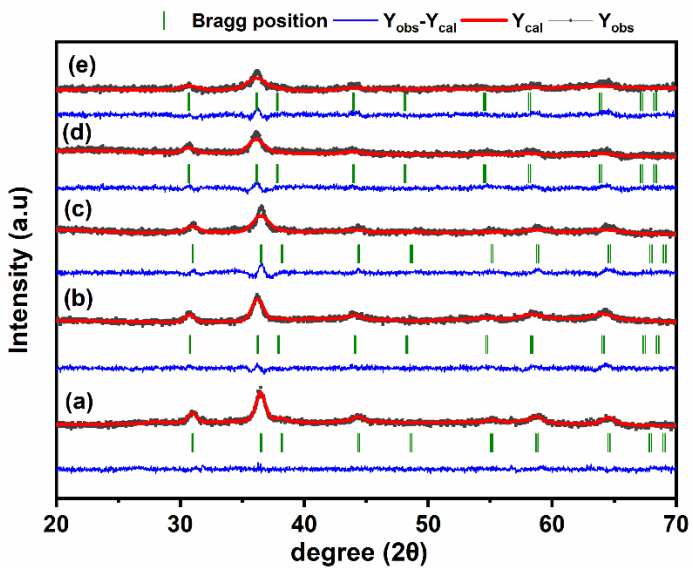


Fig. 2. Rietveld refinement profile of $Co_{0.5}Zn_{0.5-x}Mg_xFe_2O_4$ ceramic with (a) x =0.1, (b) x =0.2, (c) x =0.3, (d) x =0.4, and (e) x =0.5

3.2. FT-IR spectroscopy

Fig. 3(a) shows Co-Zn ferrites and Mg doped Co-Zn ferrites noted between 4000–400 cm^{-1}. In higher wave number region, the band seen in 3648–3665 cm^{-1} correspond to the bond vibrations of O–H groups arising from both free and bound water molecules. The band appearing near 2322–2327 cm^{-1} pointing to the occurance of atmospheric CO_2 adsorbed on the ferrite surface while, the band located over the interval 1618–1629 cm^{-1} are characteristics of H-O-H bonds, reflecting the absorbed water molecules [16, 28]. The two metal oxides show distinct absorption bands v_1 and v_2 attributable to M–O vibrational modes are detected within the 400–600cm^{-1} [12]. The higher-frequency region (v_1) appearing detected in 651–659 cm^{-1} is attributed to the bond vibration of M-O bonds at the tetrahedrally coordination which exhibit shorter bond length, whereas the lower-frequency region (v_2) observed between 450–486 cm^{-1} corresponds to M-O bond vibration at octahedrally coordination characterized by longer bond length. In this spectra, a slight shift of both v_1 and v_2 bands toward higher wavenumbers is observed with increasing Mg content confirming the cations distributes across both tetrahedrally and octahedrally coordination. The observed shift toward higher frequencies is generally associated enhanced Fe^{3+}–O^{2-} bonding interactions. [29]

The values of the force constants at octahedrally (B) and tetrahedrally (A) coordination were estimated according to the below relations [30, 31]:

$$k_o = 4\pi^2 c^2 v_1^2 \mu \qquad (6)$$

$$k_t = 4\pi^2 c^2 v_2^2 \mu \qquad (7)$$

c refers to speed of light, v_1 and v_2 correspond to stretching frequency, μ refers to reduced mass of M-O bond, calculated based on redistributed cations is equal to 2.061×10^{-23} g

The metal–oxygen bond lengths at the tetrahedrally and octahedrally coordinated position were evaluated by correlating the calculated force constants using the relation reported with literature [32, 33]:

$$r_{t/o} = \left(\frac{17}{k}\right)^{\frac{1}{3}} \qquad (8)$$

Here, k_t is greater than k_o for all Mg substituted ceramics as shown in table S2, indicating stronger metal–oxygen bonding at tetrahedral sites. With increasing Mg content, k_o shows increases particularly at x=0.2 sample, indicating that the Mg substituted sample influences the octahedral sublattice. This variation can be linked to occupation of Mg^{2+} ions at octahedrally coordination, which induces cation redistribution and pushing Fe^{3+} ions toward tetrahedrally coordination. The increase of k_t with Mg content confirms the improved Fe^{3+}-O^{2-} interactions at tetrahedral sites, resulting in increased force constants and stronger bonding. The bond lengths shows an opposite trend to the force constants, where the octahedral bond length (r_o) reduces from 2.259 Å−2.213 Å with increasing Mg content, while the tetrahedral bond length (r_t) shows a slight decrease from 1.766 Å−1.753 Å. The variation in force constant is inversely related to bond length confirm stronger bonding is associated with shorter metal–oxygen distances. The decrease in bond lengths indicates that stronger chemical bonds have resulted in lattice contraction and an increase in bond stiffness due to Mg^{2+} induced cation redistribution within the spinel lattice which is consistent with XRD results showing enhanced crystallinity.

Debye temperature (θ_D) are physical factor for understanding lattice dynamics in solids. It denotes temperature corresponding to the greater lattice vibrational frequencies and commonly used to describe and estimate thermal properties, including specific heat capacity. The θ_D can be evaluated following relation [34]:

$$\theta_D = \frac{\hbar c v_{av}}{k_B} \qquad (9)$$

where $\hbar$, v_{av}, k_B, c represents Planck's constant, average wavenumber, Boltzmann's constant and speed of the light. θ_D increases from 789 K to 816 K in intermediate Mg content, it

remains higher than the undoped sample for all Mg doped Co-Zn ferrite compositions. This increase in θ_D indicates greater lattice stiffness due to stronger metal–oxygen interactions and better crystallinity [35].

3.3. DRS analysis

Fig. 3(b-g) shown UV–Vis DRS were investigate the energy band gap for $Co_{0.5}Zn_{0.5-x}Mg_xFe_2O_4$ where (x = 0.0–0.5) noted over the spectral interval between 300–1200 nm and to understand the impact of crystal size and Mg substitution on their optical behavior. The band gap energy (E_g) of the samples were estimated from Kubelka-Munk method [28]:

$$F(R) = \alpha = \frac{(1-R^2)}{2R} \quad (10)$$

Here R is reflected light (%) and α represent co-efficient of absorption which is important to see the absorption capacity of a material under a photon energy (hv). It is related to the optical band gap E_g which is minimum amount of energy that an electron need to be transform from the valence band (VB) to conduction band (CB) in a semiconductor. The band gap energy is core property that strongly influences both optical and electrical performance of the ceramics.

All the samples shows lower reflectance in the UV and visible regions, followed by a increase toward the near-infrared (NIR) region, which is a common optical behaviour of cubic spinel ferrites [36, 37]. For undoped Co-Zn ferrties shows significant increase in reflectance in the NIR range (800–1100 nm), reaching a maximum reflectance of ~38%. This increased reflectance in the NIR region because of their higher concentration of Co^{2+} and Zn^{2+} ions and their corresponding electronic transitions along with reduced lattice disorder in the undoped composition. A gradual increase in overall reflectance is seen throughout the entire spectral range particularly in the NIR region, with rising substitution of Mg doped samples (x=0.1 to x=0.5). The observed trend implies electronic configuration and reduced light absorption due to Mg incorporation. Since Mg^{2+} is a non-magnetic ion with a closed-shell electronic configuration, its substitution reduce the contribution of d–d transitions associated with Co^{2+} ions, leading to low reflectance. In the UV–visible range (300–700 nm), all samples doped by Mg^{2+} ion shows low reflectance values, indicates strong absorption of incident light [38]. This enhanced absorption is likely related arising from charge transfer interaction between O^{2-} and Fe^{3+} species and intervalence charge transfer in Fe^{2+}/Fe^{3+} species at octahedrally coordination.

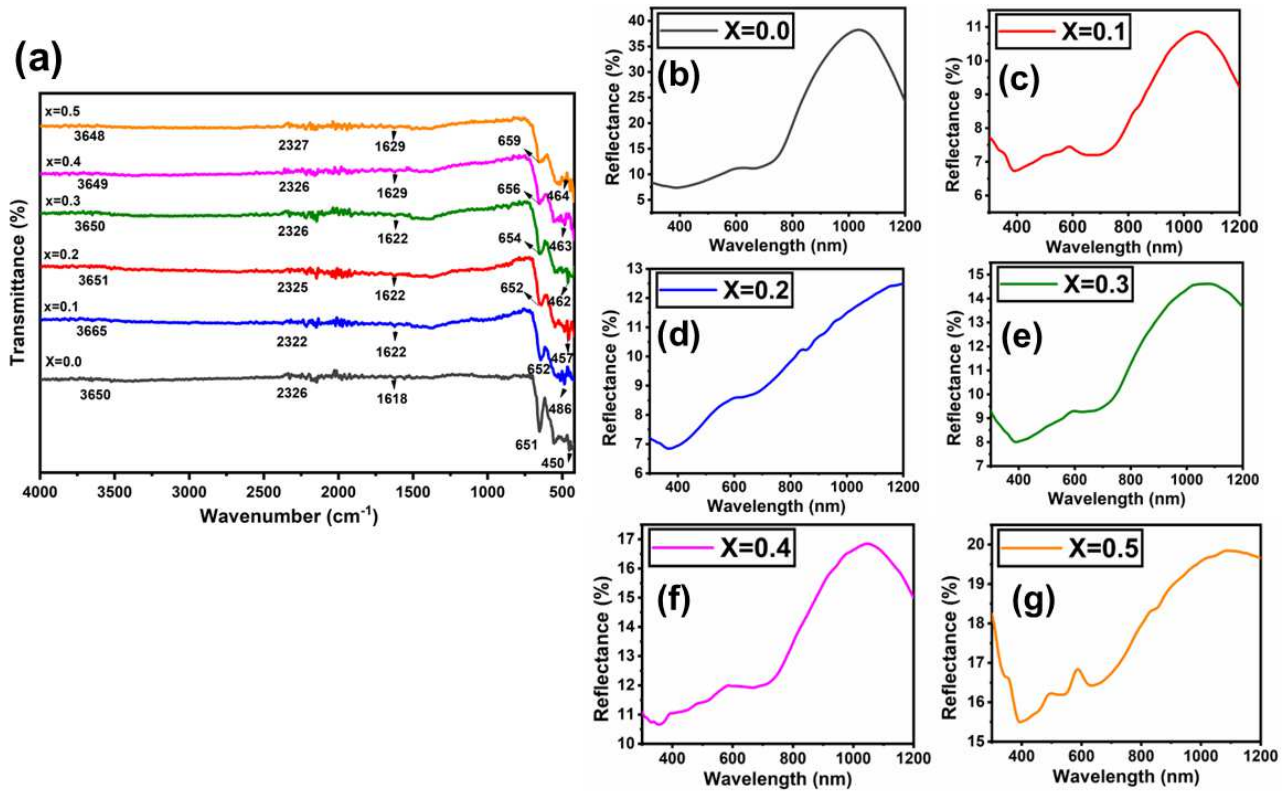


Fig. 3. **(a)** FT-IR spectra and **(b-h)** DRS analysis of $Co_{0.5}Zn_{0.5-x}Mg_xFe_2O_4$ (x = 0.0–0.5) ceramics.

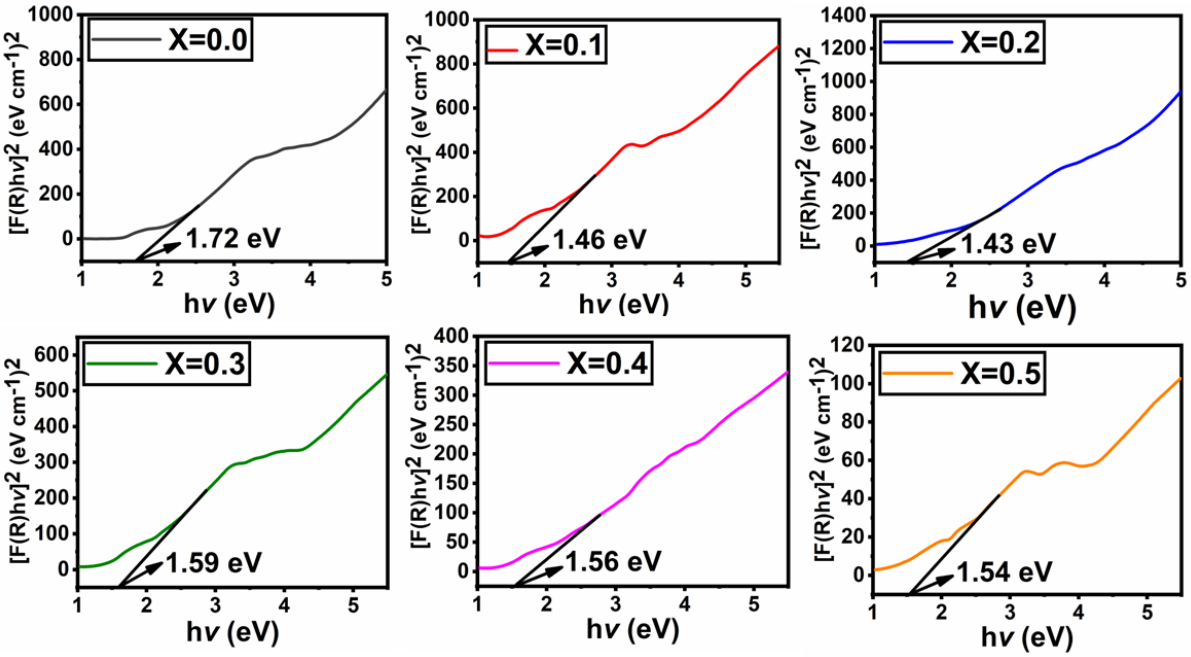


Fig. 4. Optical band gap energy from Kubelka-Munk plot for $Co_{0.5}Zn_{0.5-x}Mg_xFe_2O_4$ (x = 0.0–0.5)

The optical band gap energies of $Co_{0.5}Zn_{0.5-x}Mg_xFe_2O_4$ (x = 0.0 – 0.5) was estimated from UV–Vis–DRS using Kubelka–Munk function to transform reflectance data into an equivalent absorbance enabling the construction of modified Tauc plots for band gap determination [16]:

$$[F(R)h\nu] = A\left(h\nu - E_g\right)^n \quad (11)$$

Here, $F(R)$ represents Kubelka–Munk function, $h\nu$ denotes photon energy, E_g correspond to optical band gap, n takes a value of 2 and ½ for direct or indirect transitions. Since both zinc and cobalt ferrites exhibit direct band gaps [39], the synthesized Co-Zn ferrite are expected to possess a direct optical band gap. The graph of $[F(R)h\nu]^2$ vs $h\nu$ for all compositions presented in Fig. 4. The optical band gap energies of the prepared ceramics were obtained by extending the linear region of $[F(R)h\nu]^2 = 0$ curve on the energy axis. The undoped sample revealed a energy gap of 1.72 eV, which is characteristic of Co-Zn ferrites and arises mainly from electronic transitions involving Fe^{3+} ions at octahedral sites. For x=0.1 (1.46 eV) and x=0.2 (1.43 eV), a initial decrease in band gap energy is noted upon Mg substitution including lattice distortion and the rearrangement of cations. A decrease in band gap with reduced crystal size is against conventional quantum confinement effects [40]. When Mg^{2+} ions get substituted in, it changes the local crystal field and it also move the Fe^{3+} ions around between the A and B coordinate positions. This creates localized energy states that are inside the forbidden gap. These defect states facilitate electronic transitions at lower photon energies, thereby reducing the band gap. Jangam et al [14]. had also mentioned this non-linear change in band gap energy with dopant concentration has been previously observed in $Zn_{1-x}Co_{0.5x}Mg_{0.5x}Fe_2O_4$ spinel ferrites, where the band gap initially decreased because of their Mg^{2+} and Co^{2+} incorporation and then it changes at higher substitution levels influenced by cation distribution and electronic state of the material.

Further Mg concentrations (x=0.3–0.5), it is seen that the band gap slight increase for x=0.3, reaching 1.59 eV, 1.56 eV, and 1.54 eV, in that order. This behavior shows some stabilization of spinel lattice at higher Mg^{2+} concentrations. Mg^{2+} ions occupied octahedral sites therby reduces Fe^{3+}–Fe^{2+} intervalence charge transfer [41]. Badiger et al. [10] have found band gap values in between 1.56–1.46 eV for Cr doped Co-Zn ferrites, which closely match the results with present study. The microstructural effects such as changes in crystal size and reduced strain may also support to this trend. A relatively low band gap values (1.43–1.59 eV) indicate enhanced visible-light absorption, making the Mg substituted Co–Zn ferrite suitable for use in optoelectronic device.

3.3.1. Refractive index (n)

The refractive index is an important optical property that describes the interaction of light with electrons in a material. It is closely correlated with the optical density and light absorption characteristics of the material. The refractive index (*n*) were evaluated by below relation,

$$E_g n^4 = K \qquad (12)$$

Here, *n* means refractive index of the semiconductor, *K* denotes constant is equal to 108 eV, and E_g represents energy band gap. In table 4, refractive index shows a non-monotonic variation with Mg concentration. The x=0.0 exhibits a lower refractive index (2.8148), which increases significantly at low Mg substitution, reaching a maximum point of 2.9479 for x=0.2. The observed enhancement related to band-gap narrowing, increased electronic polarizability, and cation redistribution induced by Mg incorporation. At higher dopant concentration, a slight decrease in *n* is observed, likely due to reduced structural disorder and improved lattice stability, which lower the materials polarizability. The observed trend confirms the strong dependence of refractive index on Mg^{2+} induced changes in the electronic features accociate with ferrite system.

3.3.2. Reflectivity (R) & Absorption coefficient (*α*)

Reflectivity is an optical measure of the amount of incident light reflected at a material's surface and is primarily determined by the refractive index and surface features. The reflectivity was calculated using following relation,

$$R = \left(\frac{n_{material} - 1}{n_{material} + 1}\right)^2 \times 100\% \qquad (13)$$

The reflectivity exibit a moderate but consistent change in rising Mg concentration (Table 4). The observed rise in reflectivity at low Mg content, which could be due to rise in refractive index and greater electronic polarizable causing stronger reflection of incident light. However on increase the amount of Mg concentration, the reflectivity slightly decrease and then remain stable, indicating improved lattice ordering and reduced polarization effects.

The absorption coefficient (α) is an important optical parameter that quantifies the amount of incident light absorbed as it propagates through a ceramic material, with higher values indicating stronger light absorption. The absorption coefficient (α) was determined from

diffuse reflectance data using the Kubelka–Munk method, providing a standard measure of light absorption per unit path length within the samples.

$$\alpha = \frac{1 - R^2}{2R} \qquad (14)$$

Where R is reflectance. The absorption coefficient (α) for Mg doped Co-Zn ferrites samples varies within a narrow range (10.337 to 11.190 cm^{-1}) as shown in Table 4. This rise in (α) seen at low Mg substitution because of higher photon absorption due to band gap narrowing and electronic transitions. As Mg substitution increases, the coefficient stabilizes and slightly reduces, a trend we associated with more ordered lattice structure and reduce defect related transitions.

3.3.3. Penetration depth (δ)

When light enters a material, some of that incoming radiation gets absorbed, and this make the light less intense. The penetration depth (δ), also referred to as the skin depth, represents the distance over which incident radiation penetrates into the material before its intensity is significantly attenuated. Initially, δ decreases from 0.0967 to 0.0893, indicating improved attenuation of electromagnetic waves within the material. After this, again slight increase (0.0927–0.0921). indicating a effective absorption by electromagnetic waves and by the material becomes more effective at intermediate compositions and remains consistent. This slight change δ indicates stable absorption behaviour , which is suitable for high-frequency device applications.

3.3.4. Molar refractive index (R_m) and Molar electronic polarizability (α_m)

The molar refractive index (R_m) and mean polarizability (α_m) of Co-Zn ferrite and Mg doped Co-Zn ferrites were tabulatd in table 4. Both R_m and α_m decrease initially up to x = 0.2 and subsequently exhibit a slight increase with further Mg^{2+} doping. This change occur due to replacement in Zn^{2+} with Mg^{2+} ions which are less polarizable. This reduces electronic cloud distortion at lower concentrations. At higher Mg contents, a small increase suggest a structural rearrangement and also stabilization of the lattice strucutre. These variations indicate changes in the electronic environment and polarizability, which influence the material's response to external fields and are important for its dielectric and optoelectronic properties.

3.3.5. Reflection Loss (R_L) and the transmission coefficient (T)

Reflection Loss (R_L) measures how much electromagnetic energy that hits a material's surface and gets reflected back. It quantifies surface-related optical losses and is commonly expressed using the Fresnel relation. The transmission coefficient (T) is defined as the ratio of transmitted to incident electromagnetic power passing through a material and serves as a measure of the material's transparency. Fig. S4 and Table 4 illustrate the variation in reflection loss (R_L) and transmission coefficient (T) with Mg doping concentration in Co–Zn ferrites. Samples that have higher refractive index show slightly more reflectance and less transmittance, while samples with lower refractive index value show reduced reflection loss and improved transmission. x=0.2 samples which have higher n show increase reflection loss and reduced transmission, indicating stronger light–matter interaction and improved surface reflectivity due to increased electronic polarizability. This results confirms that the Mg substitution effectively modulates the optical response of the ceramic material.

Table 4

Optical and electronic properties for $Co_{0.5}Zn_{0.5-x}Mg_xFe_2O_4$ (x=0.0-0.5) ceramics.

Sample code	**x = 0.0**	**x = 0.1**	**x = 0.2**	**x = 0.3**	**x = 0.4**	**x = 0.5**
E_g (eV)	1.72	1.46	1.43	1.59	1.56	1.54
Refractive index (n)	2.8148	2.9326	2.9479	2.8708	2.8845	2.8938
Reflectivity (R%)	22.63	24.15	24.34	23.35	23.53	23.65
Absorption coefficient (α) (cm^{-1})	10.337	11.095	11.190	10.696	10.786	10.846
Penetration depth (δ) (cm)	0.0967	0.0901	0.0893	0.0934	0.0927	0.0921
Molar Refractive Index (R_m) (cm^3/mol)	34.684	34.137	33.012	33.913	34.098	34.187
Molar Electronic Polarizability (α_m) $(Å)^3$	13.763	13.546	13.100	13.457	13.530	13.566
Reflection Loss (R_L)	0.2263	0.2415	0.2436	0.2337	0.2353	0.2366
Transmission co-efficient	0.6310	0.6110	0.6086	0.6211	0.6186	0.6174

(T)						

3.4.Magnetic property

The room temperature magnetic hysteresis loop of the synthesized $Co_{0.5}Zn_{0.5-x}Mg_xFe_2O_4$ (x = 0.0 to 0.5) ceramics were presented in Fig. 5(a). The obtained hysteresis loops confirm that all samples exhibit ferromagnetic behavior, characterized by non-zero saturation magnetization (M_s), remanence (M_r), and coercive field (H_c) in Table 5 and Variation of these parameters are shown in Fig. S5 (a) & (b). In addition to these parameters, the squareness ratio $R = (M_r/M_s)$, Bohr magneton $\mu_B = M_s/5585$, and magnetic anisotropy constant $K = H_c M_s/0.96$ were evaluated to understand the magnetic characteristics more comprehensively. These parameters provide insight into the magnetization retention, magnetic moment per formula unit, and the energy required for magnetization, respectively. Magnetization characteristics are grouped under three groups as reported in the magnitude of their coercive field (H_c) is hard (above 800 Oe), semi-hard (511–800 Oe) and (below 511 Oe) soft magnetic materials. The narrow loops with low H_c indicate that the prepared Mg doped Co-Zn ferrites possess soft ferromagnetic nature [42]. The observed ferromagnetic and multidomain nature is observed in present study are in good aggrement reported by Abu Elsaad et al. [27] for $Mn_{0.4}Zn_{0.6-x}Cu_xFe_2O_4$ ferrite and Jangam et al. [14] for $Zn_{1-x}Co_{0.5x}Mg_{0.5x}Fe_2O_4$.

Initially, M_s increases from x = 0.0 to x = 0.1 and then exhibits a slight reduction in the x=0.2 (0.745 emu/g), and then a significant increase for higher Mg concentrations, rising to 3.1784 emu/g in x=0.5. The observed trend is caused by redistributed cations among tetrahedrally and octahedrally coordination in the lattice. Neel's theory describes three possible superexhange mechanism namely A–B, A–A, and B–B interactions, of these A−B coupling possesses the greatest strength and primarily governs the magnetic response of ferrites.

In Mg substituted Co-Zn ferrites, Zn^{2+} ions are no intrinsic magnetic moment and are mainly located at the tetrahedrally coordination which are preferred for A-site, resulting in a reduced A-sublattice magnetic moment (M_A). The total magnetic response is governed by the difference in magnetization accociated with octahedrally and tetrahedrally coordination (M = M_A-M_B). When Mg^{2+} replaces Zn^{2+}, the distribution of cations changes because Mg^{2+} ion can occupy both A and B coordination. This causes a redistribution of Fe^{3+} ions between the tetrahedral (A) and octahedral (B) sublattices, thereby affecting the strength of the A–B

superexchange interactions [7]. In initial increase in M_S from x = 0.0 and x = 0.1 enhanced A-B superexchange interactions resulting from a minor rearrangement of Fe^{3+}, which increases the overall magnetic moment. The reduction observed for the x = 0.2 can be associated with diminished inter sub-lattice A–B interactions or development of spin misalignment at B-sites, which reduces the effective magnetic moment. At higher Mg content (x ≥ 0.3), improved alignment of magnetic moments and dominant B-site contribution result in a significant increase in M_S. A similar non-linear variation in M_S and H_c with Mg^{2+} substitution has been reported by Islam et al. [5] in $Zn_{0.6}Cu_{0.4-x}Mg_xFe_2O_4$ ferrites, where the initial increase is attributed to enhanced A–B superexchange interaction, followed by a decrease due to magnetic dilution effects.

The M_r remains very low within low Mg substitution x = 0.0 to 0.2 indicating weak magnetic retention and suggesting the presence of multi-domain behavior due to small particle size or thermal fluctuations. As Mg content rises x = 0.3 to 0.5, (M_r) increases, indicating improved magnetic ordering and domain stability. The ratio of (M_r/M_s) provides information about domain arrangement within the material. When the ratio is less than 0.1, it suggest a multi-domain state where magnetization happen through domain wall motion. When the ratio is greater than 0.5, it indicate single-domain behaviour, where magnetization is controlled by spin rotation. Values between 0.1 to 0.5 is a pseudo-single domain structure. In all samples, the ratio remains very low (R ≈ 0.0023–0.0349; $M_r/M_s < 0.01$), confirm that there is no long range ferromagnetic ordering. The very low ratios observed clearly shows that the material is multi domain soft magnetic properties [42].

As the Mg content increases, the value of H_c slightly rise reaching a Mg content of x = 0.2 after which it reduces at higher levels of Mg. This trend is affected by multiple factors such as the size of the crystallites, redistributed of cations within the crystal structure and the magnetocystalline anisotropy. X-ray diffraction results indicate an initial reduction in crystallite size which subsequently rises as the Mg substitution. Since the ceramics exhibit multi-domain behavior, the increase in crystallite size at higher Mg content facilitates domain wall motion, leading to a reduction in coercive field. The smallest H_c is associate with the sample (x = 0.5). A systematic decrease in H_c with increasing Mg substitution indicates a reduced resistance to demagnetization under an applied magnetic field. The reduced magnetocrystalline anisotropy allows easier domain wall motion and magnetization reversal. Additionally, the decrease in anisotropy (K) due to Mg substitution allows magnetic moments to realign more easily, resulting in decreased coercive field [43, 44]. The ferromagnetic

behavior exhibited by the sample have been described in earlier reports on $Cr_xZn_{0.5}Co_{0.5}Fe_{2-x}O_4$ ferrites, where comparable values of H_c and (M_r/M_s) were observed [45]. In conclusion, based on the obtained magnetic parameters, particularly low coercive field, low (M_r/M_s) ratio, and reduced anisotropy, the synthesized ceramic ferrites demonstrate potential suitability for magnetic recording media and high-frequency device applications.

Further analysis of the switching field distribution (SFD), derived from the dM/dH versus H curves shown in Fig. 5(b), provides valuable information on the magnetization reversal process and the domain structure of the samples. The differential magnetization (dM/dH) curve exhibits a single peak centered at zero magnetic field. This feature indicates a uniform magnetization reversal process without significant magnetic phase separation. The absence of multiple peaks suggests magnetic homogeneity, confirming the soft magnetic nature of the prepared ferrites. It is observed that the height of the peak is raised with higher Mg doping concentration, indicating improved magnetic response of the ferrites. The peak reaches its highest point when the Mg content is at x = 0.5, which correspond to the highest saturation magnetization and lowest coercive field. This make the magnetization reversal is getting easier and also more coherent with increasing Mg content. The SFD peak become narrower when more Mg substitutes into the material. This point is to more uniform way the switching fields are distributed. This improvement is likely due to better magnetic homogeneity and reduced anisotropy. These characteristics make this material suitable for high-frequency device and magnetic recording media applications.

Table 5

Room-temperature magnetic properties of $Co_{0.5}Mg_xCu_{0.5-x}Fe_2O_4$ (x = 0.0–0.5).

Sample code	**M_s**	**M_r**	**H_c**	**n_B (μ_B)**	**$\frac{M_r}{M_s}$**	**K**
x = 0.0	0.656	0.0139	56.135	0.0279	0.0211	38.358
x = 0.1	0.8428	0.0019	62.682	0.0352	0.0023	55.225
x = 0.2	0.745	0.0051	64.348	0.0306	0.0068	49.936
x = 0.3	1.2427	0.0248	13.063	0.0501	0.0199	16.909
x = 0.4	2.2591	0.0348	13.760	0.0895	0.0154	32.38
x = 0.5	3.1784	0.1110	1.7063	0.1236	0.0349	5.649

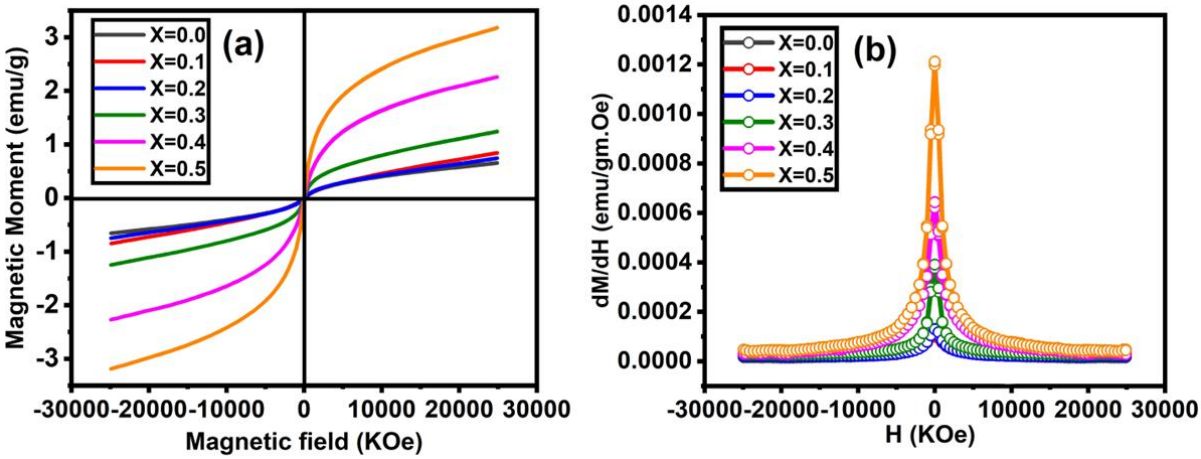


Fig. 5. **(a)** Magnetic hysteresis loops of $Co_{0.5}Zn_{0.5-x}Mg_xFe_2O_4$ (x = 0.0-0.5) at room temperature; **(b)** corresponding dM/dH versus H curves showing the switching field distribution (SFD).

3.5.Electrical property analysis

3.5.1. Dielectric analysis

Fig. 6 presents the variation of the dielectric constant (ε′) for $Co_{0.5}Zn_{0.5-x}Mg_xFe_2O_4$ (x= 0.0–0.5) ceramic compositions measured over the frequency range of 1 Hz to 7 MHz. As shown in Fig. 6, the ε′ of all prepared ceramic compositions is high at low frequencies, decreases sharply with increasing frequency, and gradually approaches a nearly constant value at higher frequencies. A similar frequency-dependent dielectric behavior has been reported for Mg–Co–Zn [15], Co–Zn–Mn [13], and Zn–Cu–Mg [5] nanoferrites. This variation can be clarify by the Maxwell–Wagner interfacial polarization mechanism as per Koops two-layer model. At lower frequency, the external electric field applied to the material allows sufficient time for charge carriers to build up grain boundaries. These boundaries are great resistive than actual grains. This buildup space charges leads to large polarization and hence ε′ is high constant values. With increasing frequency, the localized charge carriers fail to respond to the rapidly varying electric field, resulting in reduced space charge polarization and a corresponding decrease in the ε′. At higher frequencies, the dielectric response is predominantly governed by electronic and ionic polarization, resulting in an almost frequency independent dielectric constant. [13]. An increase in temperature generally enhances the dielectric constant (ε′), particularly in the low-frequency region. This behavior is attributed to thermally activated electron hopping between Fe^{2+} and Fe^{3+} ions at the octahedral (B) sites, which increases space charge polarization and consequently enhances the dielectric constant. An increase in temperature enhances the mobility of charge carriers, leading to a decrease in

intergranular resistance and an increase in interfacial polarization [36]. However, at higher frequencies, the influence of temperature becomes less significant because the dipoles are unable to respond to the rapidly alternating AC electric field. Therefore, the observed increase in the dielectric constant (ε′) with temperature confirms that thermally activated hopping conduction is the dominant polarization mechanism in the prepared ferrites.

Undoped Co-Zn ferrite shows low dielectric constant, with ε′ around 700–800 at low frequency and decreasing to ~100 at higher frequencies with normal dispersion behavior. With the initial Mg content is x = 0.1, ε′ value reachs on the order of 10^5 which is higher than that of the undoped Co-Zn ferrite indicating strong interfacial polarization effects. For the x = 0.2 sample, the dielectric constant (ε′) remains relatively high in the low-frequency region and decreases rapidly with increasing frequency, reaching a low value at higher frequencies. This behavior indicates strong space charge polarization at low frequencies, while the reduced dielectric response at higher frequencies suggests that the polarization mechanism becomes less responsive to temperature variations. For the x = 0.2 sample, the dielectric constant (ε′) remains relatively high in the low-frequency region and decreases rapidly with increasing frequency, reaching a low value at higher frequencies. This behavior indicates strong space charge polarization at low frequencies, while the reduced dielectric response at higher frequencies suggests that the polarization mechanism becomes less responsive to temperature variations. For the x = 0.3 and x = 0.4 compositions, the dielectric constant (ε′) decreases compared with the x = 0.1 and x = 0.2 samples, exhibiting maximum values in the range of 10^4–10^5 along with comparatively lower dielectric dispersion. The x = 0.5 ferrite exhibits the highest dielectric constant among all compositions, reaching approximately 10^5 in the low-frequency region and showing pronounced dielectric dispersion. The observed dependence on ε' on Mg content indicate the influence of compositional changes on the microstructural features and build up of charges at interface, which affect response of $Co_{0.5}Zn_{0.5-x}Mg_xFe_2O_4$ ferrites. These results correlate earlier sudies on the dielectric behavior of chemical co-precipitation method derived Co-Mn-Zn nanoferrites by Fadafan et al. [18].

Fig. 7 shows the frequency dependence of the dielectric loss (ε″) for $Co_{0.5}Zn_{0.5-x}Mg_xFe_2O_4$ (x=0.0–0.5) ceramics. All compositions exhibit a pronounced frequency-dependent dielectric loss behavior. In every sample, dielectric loss is significantly high in the lower frequency and decreasing rapidly with increased frequency, eventually approaching zero at high frequency. The ε'' trend is like to ε' because of charge accumulation at boundaries and charge carrier hopping, where accumulated charges at boundaries contribute to greater energy loss. ε″

significantly reduced along increased frequency tells us about Maxwell–Wagner interfacial polarization mechanism [46]. For undoped Co-Zn ferrtie (x=0.0), the ε″ values are very small even at high temperature and are approximately 10^{-4}-10^{-3} and have decreases to ~3.45×10^{-4} at high frequencies (200 ^{o}C) indicating the low energy dissipation and stable polarization behaviour. The anomalous increase in ε″ with Mg substitution at x=0.1 and 0.2 is observed in small frequency values close to ~0.4 and ~0.8, while the loss decrease at high frequencies to ~2.98×10^{-7} (x=0.1) and 1.92×10^{-7} (x=0.2) depending on temperature which is attributed to charge carrier hopping. The dielectric loss for intermediate composition x=0.3 is lower than that for x=0.1 and x=0.2 and is stable at ~1.4×10^{-7} at higher temperature, indicating a lower energy dissipation and reduced defect dipole interaction. The x=0.4 content shows a slight increase, although strong frequency dispersion remains. At x = 0.5, the dielectric loss (ε″) again increases at low frequencies, reaching approximately 0.8 at 1 Hz, suggesting enhanced defect-induced polarization and thermally activated hopping conduction. Temperature also has a significant influence on the energy dissipation behavior of the material. For all compositions, ε″ increases with increasing temperature, particularly in the low-frequency region. This behavior is attributed to the enhanced mobility of charge carriers and increased hopping probability between localized states at elevated temperatures, resulting in greater dielectric energy loss. However, with increasing frequency, ε″ decreases because the dipoles and charge carriers cannot respond to the rapidly alternating electric field. This behavior is characteristic of Maxwell–Wagner interfacial polarization, where the contribution of interfacial charge accumulation becomes negligible at higher frequencies, resulting in reduced dielectric loss. Initial Mg substitution enhances dielectric loss at low frequencies (x = 0.1 and 0.2) due to increased Fe^{2+}/Fe^{3+} hopping and defect formation. At high frequencies, all compositions exhibit very low ε″ values (~10^{-7}), confirming good dielectric stability and low energy dissipation.

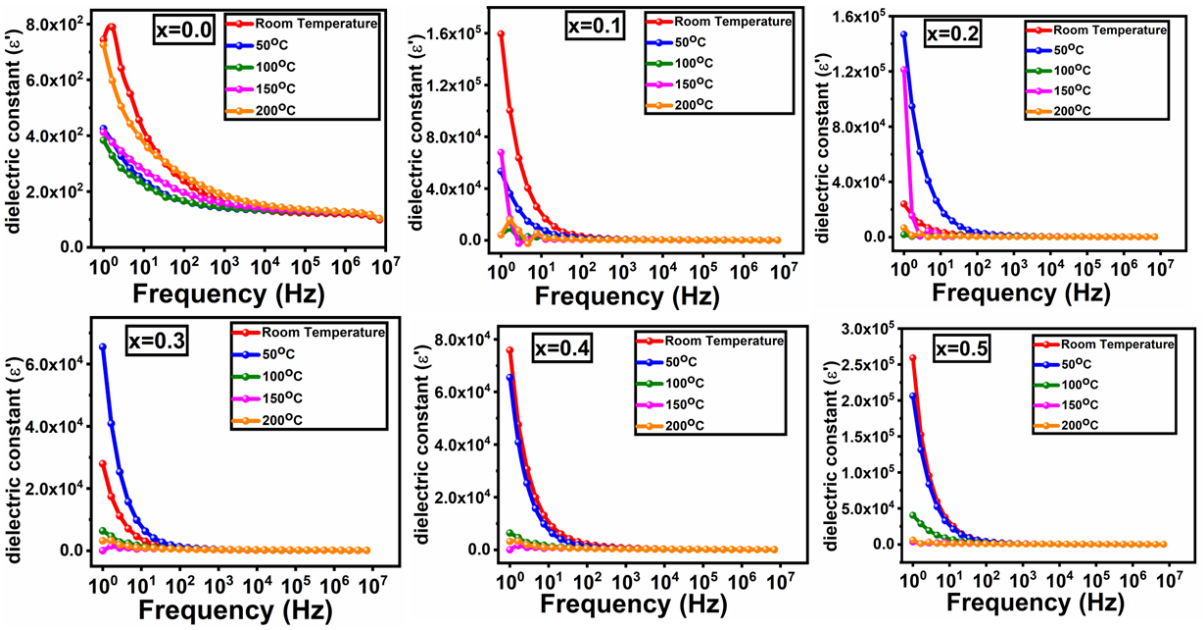


Fig. 6. Effect of frequency on ε′ of $Co_{0.5}Zn_{0.5-x}Mg_xFe_2O_4$ (x =0.0–0.5) ceramics.

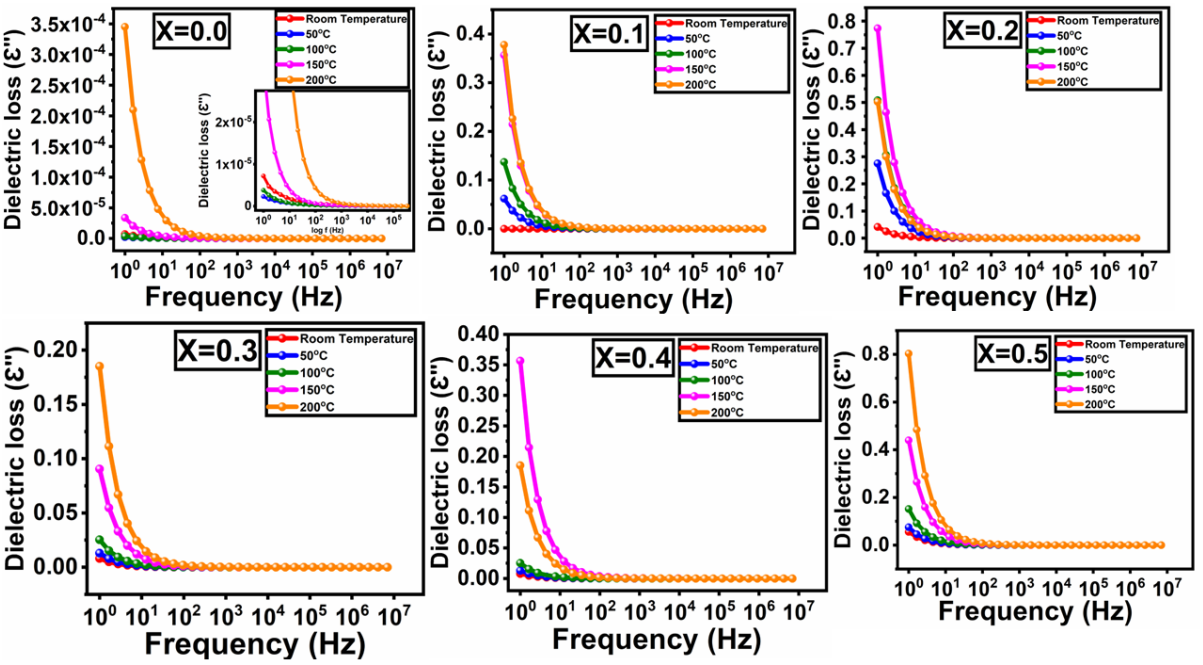


Fig. 7. Effect of frequency on ε″ of $Co_{0.5}Zn_{0.5-x}Mg_xFe_2O_4$ (x =0.0–0.5) ceramics.

3.5.2. Electrical impedance analysis

3.5.2.1. Real impedance (Z′)

The real impedance (Z′) for $Co_{0.5}Zn_{0.5-x}Mg_xFe_2O_4$ (x = 0.0–0.5) is illustrate in Fig. 8. Every ceramics exhibits a greater value on lower frequency and reduces rapidly along increased frequency, eventually to saturate at high frequency interval. A large Z′ at reduced frequency mainly related to dominant contribution of boundaries between grain, where charge carriers experience higher resistance. With increased frequency, the value of Z′

reduces as the charge carriers hop more efficiently between Fe^{2+}/Fe^{3+} ions, which leads to an improved electrical conduction. The magnitude of Z′ is seen to be strongly dependent on both frequency and composition. As the frequency rises, the Z′ reduced because of enhanced hopping of charge carriers between Fe^{2+} and Fe^{3+} ions, which improves the electrical conduction. It is found that magnitude of Z′ is dependence on frequency and composition. Among all compositions, the undoped sample (x = 0.0) exhibits the greater impedance of the order of 10^8 Ω in the low-frequency interval, implies strong intergranular resistance. With the substitution of Mg^{2+}, x = 0.1 and x = 0.2, the Z′ values reduced significantly of the order of 10^4 Ω, suggesting an improvement in charge carrier hopping and electrical conduction. While, x = 0.3 and x = 0.4, the impedance again rises, may be changes in redistributed cations and increased scattering of charge carriers at the intergranular region. However, at x = 0.5 the impedance decreases, suggest that enhanced movement of charges and reduced resistance. For all samples Z′ reduces as temperature and frequency rises, which shows that the temperature assisted conduction. At high frequency, the Z′ for different temperature tend to look similar because reduced influence of interfacial polarization and resistance at grain interface. A present result for Mg doped Co-Zn ferrite are agree with previous report on spinel ferrite [6].

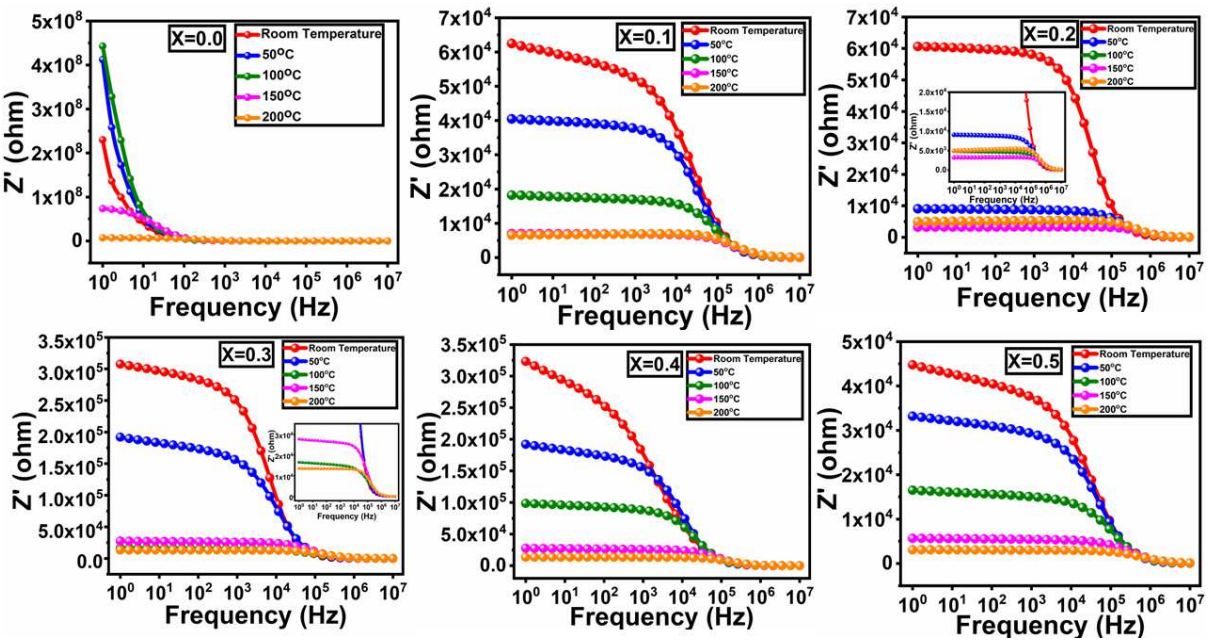


Fig. 8. Effect of frequency on Z ′ of $Co_{0.5}Zn_{0.5-x}Mg_xFe_2O_4$ (x =0.0–0.5) ceramics.

3.5.2.2. Imaginary impedance (Z″)

Fig. 9 presents imaginary component (Z″) of impedance with frequency dependent of $Co_{0.5}Zn_{0.5-x}Mg_xFe_2O_4$ (x = 0.0–0.5) at different temperature. The Z″ spectra exhibit a

characteristic peak at intermediate frequencies for most compositions, which corresponds to the relaxation process of charge carriers and the highest Z″ peak position is seen at room temperature. A undoped sample (x = 0.0), Z″ reduced monotonically with rising frequency without a well-defined peak, suggesting that the relaxation process occurs at frequencies higher than the measured range. In contrast, Mg substituted samples (x = 0.1–0.5) clearly shows relaxation peaks in the intermediate frequency region, indicating thermally activated relaxation processes. The highest Z″ peak is observed for x = 0.3 (~10^5 Ω), followed by x = 0.4 (~10^4 Ω), whereas lower peaks found at x = 0.1, 0.2, and 0.5 (~10^3–10^4 Ω). The decline in the maximum Z″ value in lowering temperature suggest a decline in the electrical resistance of all ceramics. This behavior may be associated with presence of interfacial polarization at the grain boundaries. A slight shift of relaxation peak move to higher frequency with rising temperature, confirming that conduction mechanism is temperature assisted activated [47]. This present Z″ response exhibits a more pronounced and well-defined relaxation peak compared to the $Cu_{1-x}Co_xFe_2O_4$ system reported by previous studies, indicating improved relaxation dynamics characteristics and electrical conduction behavior [48].

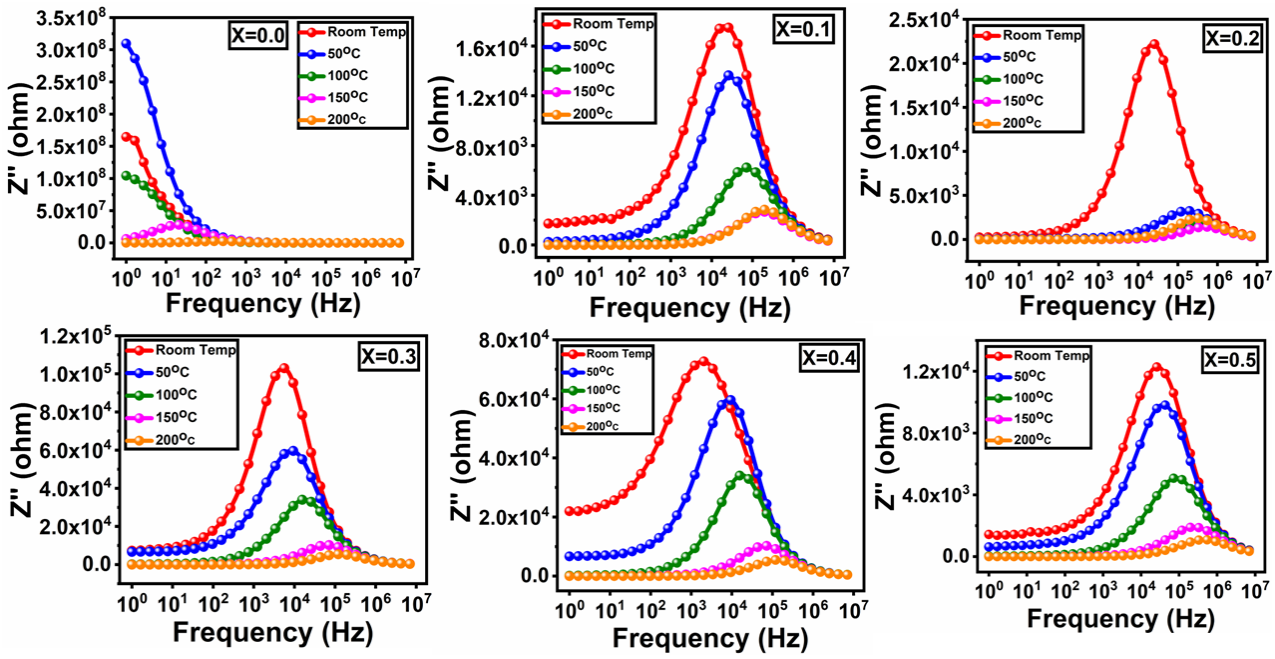


Fig. 9. Effect of frequency on Z″ of $Co_{0.5}Zn_{0.5-x}Mg_xFe_2O_4$ (x =0.0–0.5) ceramics.

3.5.3. Nyquist plot (Z′vs Z″)

Fig. 10 shows the Nyquist plots of $Co_{0.5}Zn_{0.5-x}Mg_xFe_2O_4$ (x = 0.0–0.5) measured at different temperatures. The impedance spectra, characterized by semicircular arcs, reveal the electrical response of the $Co_{0.5}Zn_{0.5-x}Mg_xFe_2O_4$ ceramics. These semicircular features arise from the combined contributions of the grain interiors (bulk) and grain boundaries

(intergranular regions) to the overall electrical transport. The distinct impedance response reflects the influence of these microstructural components on the conduction mechanism and charge carrier dynamics. Semicircle arcs exhibit largest diameter at room temperature and gradually decreases with increasing temperature for all prepared ferrites. This reduction in arc diameter suggests a decrease in bulk resistance and an improvement in electrical conductivity due to the thermally activated hopping of charge carriers. For undoped sample (x = 0.0), a very large and incomplete semicircle is observed, indicating high resistance and dominant intergranular effects. For x = 0.1 and x = 0.2, better semicircular arcs are seen. A reduction in semicircle arc diameter is observed with rising temperature showing that the bulk resistance is going down and material conductivity is better because of thermally activated conduction process, where charge carrier get enough energy to move between specific energy level. For x = 0.1, the arcs observed at 150 °C and 200 °C are overlapping suggest that the charge transport mechanism becomes more stable at higher temperatures. The size of the semicircles increases for x = 0.3 and 0.4 with respect to lower concenrations indicating higher resistance probably due to lattice distortion and the formation of defects because there is more Mg substitution which then prevents the free migration of mobile charge species. For x =0.5, impedence values are again lower than the intermediate compositions indicating improvement in conductivity. This behavior may be changes in redistributed cations and modification of microstructural features of ferrite system. $Co_{0.5}Zn_{0.5-x}Mg_xFe_2O_4$ exhibit clear relaxation behavior and strong compositional dependence, characterized by variations in semicircular arcs and temperature-dependent impedance. Similarly, Mahmood et al. [49] has been reported for $Ni_{0.80-x}Cu_{0.20}Zn_xFe_2O_4$ ferrites, where one semicircular arc in Nyquist plot suggests that electrically conduction are mainly controlled by grain-boundary characteristics. Zaman et al. [50] reported that $Sn_{1-x}Cr_xFe_2O_4$ exhibits a highly depressed or nearly linear Nyquist response, suggesting dominant interfacial polarization and grain boundary contributions. However, the present system displays well-defined semicircular arcs, confirming a dominant grain-controlled conduction mechanism with relatively uniform relaxation and reduced interfacial effects. The gradual variation in the electrical properties with increasing Mg substitution highlights the tunability of the $Co_{0.5}Zn_{0.5-x}Mg_xFe_2O_4$ ceramics, demonstrating their potential for energy storage and high-frequency electronic device applications.

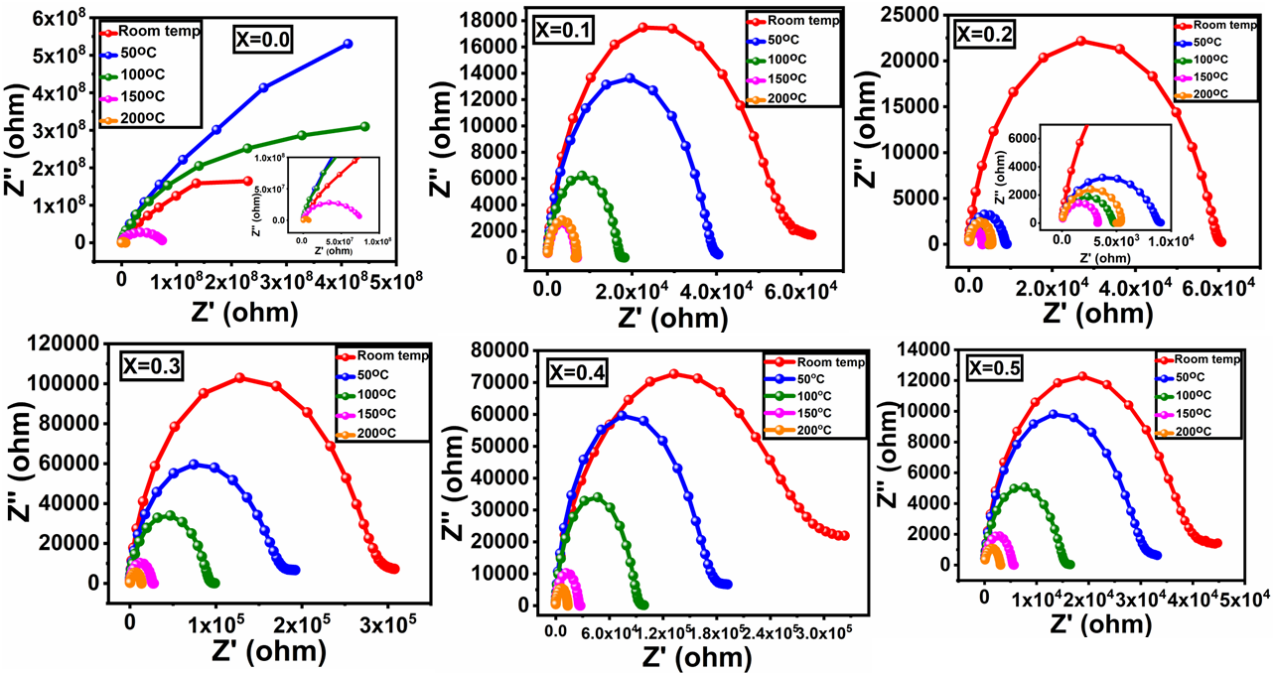


Fig. 10. Complex impedence Nyquist plot (Z′ vs Z′′) of $Co_{0.5}Zn_{0.5-x}Mg_xFe_2O_4$ (x =0.0–0.5) ceramics.

3.5.4. Electric modulus analysis

3.5.4.1. Real electric modulus (M′)

Fig. 11 represents real elastic moduls (M′) for $Co_{0.5}Zn_{0.5-x}Mg_xFe_2O_4$ (x = 0.0−0.5) as a function of frequency at various temperatures. In low frequency region M′ values for all compositions are found to be close to zero and increases with rising frequencies. The modulus values are small at low frequency implies electrode interface effect does not have much effect here. It also suggest that charge carriers can travel through material over considerable distance. As the frequency increases, migration of charge carrier start to move in localized way, this makes M′ gradually increases. For x = 0.0, there is a very sharp rise at higher frequencies and it reaches a higher saturation value indicates improves bulk conduction. For the Mg doped Co-Zn ferrites, the sharper transition in M′ indicates the predominace of bulk relaxation, which may be attributed to improved microstructural uniformity and enhanced structural homogeneity with increasing Mg concentration. This kind of behavious has been noted in other spinel ferrites like Mg doped ZCFAO ($Zn_{0.3-x}Mg_xCu_{0.7}Al_{0.3}Fe_{1.7}O_4$) [36], $LiMn_{0.5}Fe_2O_4$ [51], $Co_{1-x}Mn_xFe_2O_4$ [52]. Overall frequency response of $Co_{0.5}Zn_{0.5-x}Mg_xFe_2O_4$ of the real component of M′supports the idea that the conduction mechanism is in dominated by transition from long-range mobility of charge carriers at low frequency to localized hopping at higher frequency interval. The consistently lower M′ values at low frequency suggest minimal electrode polarization, while

the gradual rise at higher frequency points to dominance of bulk relaxation process. The effect of Mg substitution systematically modifies the relaxation dynamics, shifting the dispersion region toward higher frequencies. This behavior also enhances the charge carrier hopping process at intermediate Mg concentrations. At higher levels of Mg substitution, the modulus arcs become sharper and the dispersion behavior becomes more stable, indicating improved microstructural uniformity and a more pronounced bulk relaxation process. Therefore, the modulus analysis highlights the significant role of Mg^{2+} substitution in modifying both the electrical relaxation behavior and the charge transport mechanism of the $Co_{0.5}Zn_{0.5-x}Mg_xFe_2O_4$ ferrite materials.

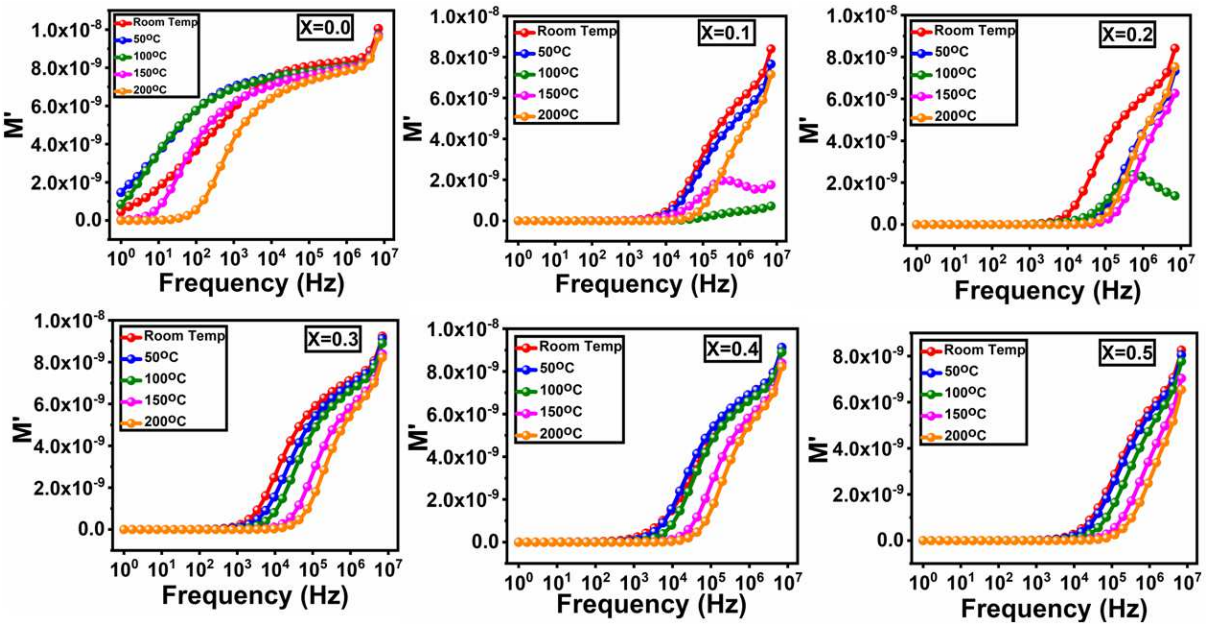


Fig. 11. Effect of frequency on M′ of $Co_{0.5}Zn_{0.5-x}Mg_xFe_2O_4$ (x =0.0–0.5) ceramics.

3.5.4.2. Imaginary electric modulus (M′′)

The temperature-dependent imaginary part of the electric modulus (M″) for $Co_{0.5}Zn_{0.5-x}Mg_xFe_2O_4$ (x = 0.0−0.5) ferrite ceramics is presented in Fig. 12. The M″ spectra provide valuable information about the electrical relaxation behavior and charge transport mechanism in the ferrite system. All compositions exhibit distinct M″ peaks, which progressively shift toward higher frequencies with increasing temperature, confirming the thermally activated nature of the relaxation process. The movement of the peaks toward higher frequencies indicates enhanced hopping of charge carriers between localized states, mainly through electron exchange between Fe^{2+} and Fe^{3+} at the octahedral (B) sites. For the undoped ferrite (x = 0.0), the M″ peak appears in the lower-frequency region and is relatively broad, indicating a broad distribution of relaxation processes associated with grain-boundary effects. As the

temperature increases, the peak gradually shifts toward higher frequencies, while its intensity initially increases and then decreases. For x = 0.1 and x = 0.2, the M″ peaks are observed at comparatively higher frequencies than those of the undoped sample, suggesting enhanced charge carrier hopping due to Mg substitution. In the x = 0.3 and x = 0.4 compositions, the peaks become sharper and more symmetrical, indicating improved microstructural homogeneity and a stronger contribution from the bulk grains. The continuous shift of the peaks toward higher frequencies with increasing temperature further confirms enhanced electrical conduction through thermally activated electron hopping. For x = 0.5, the M″ peak remains in the higher-frequency region over the entire temperature range, demonstrating efficient thermally assisted charge transport and improved electrical conductivity. Therefore, Mg substitution systematically modifies the modulus response by shifting the dispersion toward higher frequencies and producing sharper relaxation peaks, reflecting improved charge transport and bulk conduction within the ferrite ceramics.

The relaxation time (τ) corresponding to each M″ peak was determined using

$$\tau = \frac{1}{2\pi f_{max}} \qquad (15)$$

where (f_{max}) is the frequency corresponding to the maximum value of M″. The calculated relaxation time values are summarized in Table 6. The relaxation time decreases continuously with increasing temperature for all compositions, confirming the thermally activated nature of the relaxation process. The τ values vary from approximately 10^{-2} to 10^{-7} s, indicating a gradual transition from slower grain-boundary relaxation at lower temperatures to faster bulk relaxation at higher temperatures. Furthermore, the reduction in τ with increasing Mg concentration demonstrates that Mg^{2+} substitution facilitates charge carrier hopping by lowering the energy barrier for electron transport, thereby enhancing carrier mobility and electrical conduction. The overall M″ analysis confirms that Mg substitution promotes non-Debye relaxation behavior and significantly improves the electrical relaxation and conduction characteristics of $Co_{0.5}Zn_{0.5-x}Mg_xFe_2O_4$ ferrite.

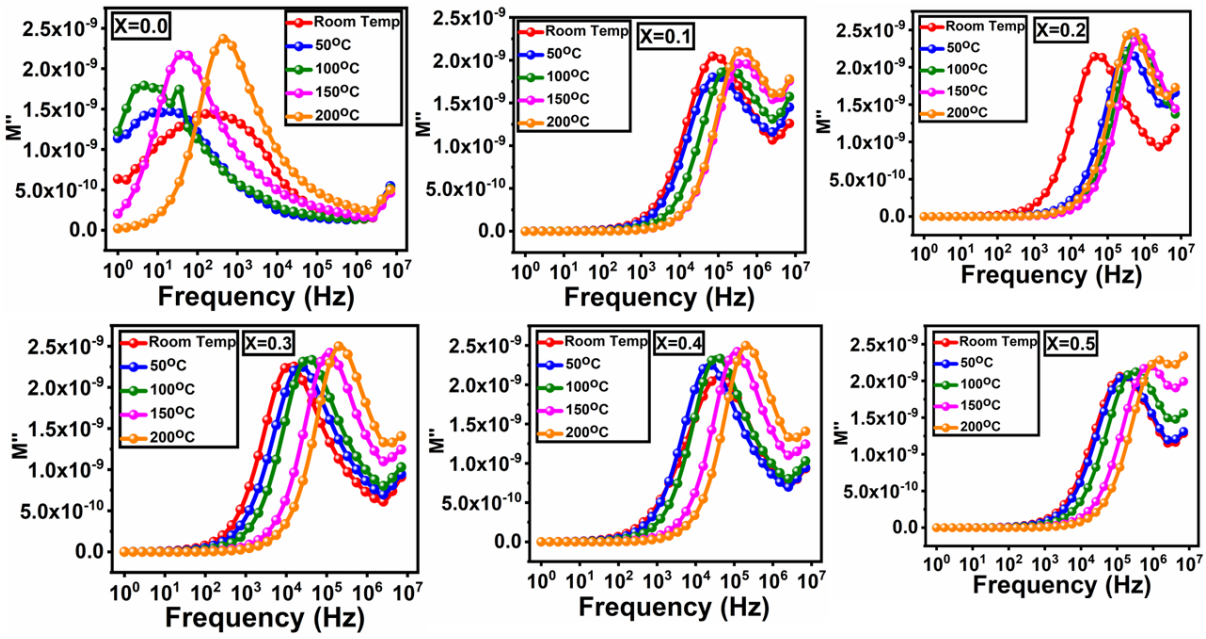


Fig. 12. Effect of frequency on M′ of $Co_{0.5}Zn_{0.5-x}Mg_xFe_2O_4$ (x =0.0–0.5) ceramics.

Table 6

Response time for $Co_{0.5}Zn_{0.5-x}Mg_xFe_2O_4$ (x =0.0–0.5) ceramics.

Temperature (°C)	Relaxation time (sec)					
	x = 0.0	x = 0.1	x = 0.2	x = 0.3	x = 0.4	x = 0.5
RT °C	7.98×10^{-4}	1.87×10^{-6}	2.90×10^{-6}	1.03×10^{-5}	3.57×10^{-6}	1.59×10^{-6}
50 °C	1.00×10^{-2}	1.91×10^{-6}	4.49×10^{-7}	6.05×10^{-6}	6.19×10^{-6}	1.42×10^{-6}
100 °C	2.19×10^{-2}	8.30×10^{-7}	2.90×10^{-7}	3.57×10^{-6}	4.1×10^{-6}	1.00×10^{-6}
150 °C	4.00×10^{-3}	4.08×10^{-7}	1.66×10^{-7}	1.36×10^{-6}	1.39×10^{-6}	5.64×10^{-7}
200 °C	3.17×10^{-4}	8.70×10^{-7}	2.64×10^{-7}	8.00×10^{-7}	7.23×10^{-7}	2.83×10^{-7}

3.5.5. Complex modulus characterstic (M′ vs M″)

The complex electric modulus (M′ versus M″) spectra of undoped and Mg doped Co-Zn ferrite measured over the frequency range of 1 Hz–7 MHz at temperatures from room temperature to 200 °C are presented in Fig. 13. The M′–M″ plots exhibit depressed semicircular arcs for all compositions, indicating a non-Debye type relaxation behavior characterized by a distribution of relaxation times rather than a single relaxation process. This behavior arises from the microstructural heterogeneity of the ferrite and the combined contributions of grain interiors and grain boundaries to the electrical conduction process. The appearance of two depressed semicircular arcs further confirms the presence of two distinct relaxation processes associated with the grain interiors in the high-frequency region and the grain boundaries in the low-frequency region. As the temperature increases, the semicircular

arcs become more pronounced and gradually contract, indicating enhanced electrical relaxation and improved mobility of thermally activated charge carriers. The reduction in the arc diameter with increasing temperature reflects a decrease in electrical resistance, confirming the negative temperature coefficient of resistance (NTCR) behavior of the ferrite ceramics. The improved conduction at elevated temperatures is attributed to the reduction in the potential barrier at the grain boundaries, which facilitates charge carrier transport throughout the microstructure.

The electrical conduction mechanism in spinel ferrites is generally explained by the small polaron hopping model, in which electrons hop between ions of the same element with different valence states. In the present Mg substituted Co–Zn ferrites, electrical conduction predominantly occurs through thermally activated electron hopping between Fe^{2+} and Fe^{3+} ions located at the octahedral (B) sites of the spinel lattice, which can be represented as

$$Fe^{2+} \rightleftharpoons Fe^{3+} + e^{-} \quad (16)$$

During this process, the electron becomes localized because of lattice distortion, forming a small polaron. As the temperature increases, sufficient thermal energy is available to overcome the hopping barrier, enabling electrons to migrate to neighboring Fe^{3+} sites. Consequently, charge carrier mobility increases, leading to enhanced electrical conduction and faster relaxation dynamics. For the undoped sample (x = 0.0), the depressed and relatively broad semicircular arc indicates a wide distribution of relaxation times resulting from the combined influence of grain interiors, grain boundaries, structural defects, and the minor secondary phases observed in the XRD analysis. At a lower Mg concentration (x = 0.1), the semicircular arc remains asymmetric, suggesting a significant contribution from grain-boundary relaxation and localized charge carrier motion. With further Mg substitution (x = 0.2–0.4), the semicircular arcs become more well-defined and approach an ideal semicircular shape, indicating that the bulk grain response gradually becomes dominant. This improvement can be attributed to the redistribution of cations caused by the substitution of Mg^{2+} for Zn^{2+}, which modifies the concentration of Fe^{2+}/Fe^{3+} pairs at the octahedral sites and enhances the probability of electron hopping. At the highest Mg concentration (x = 0.5), the semicircular arc becomes broader again, indicating a wider distribution of relaxation times due to increased lattice disorder and structural distortion introduced by the higher dopant concentration. Collectively, the evolution of the modulus spectra with increasing temperature and Mg substitution demonstrates the coexistence of grain and grain-boundary relaxation

processes, with a gradual transition toward dominant bulk conduction at intermediate Mg concentrations. The observed non-Debye relaxation behavior and NTCR characteristics are consistent with the Maxwell–Wagner interfacial polarization model commonly reported for heterogeneous polycrystalline ferrites. Similar electrical relaxation behavior has been reported for $Pb_{1-x}Sm_x(Zr_{0.55}Ti_{0.45})_{1-x/4}O_3$ [53] and $Ni_{0.27}Cu_{0.10}Zn_{0.63}Fe_2O_4$ [6], where grain and grain-boundary contributions govern the electrical relaxation and conduction mechanisms.

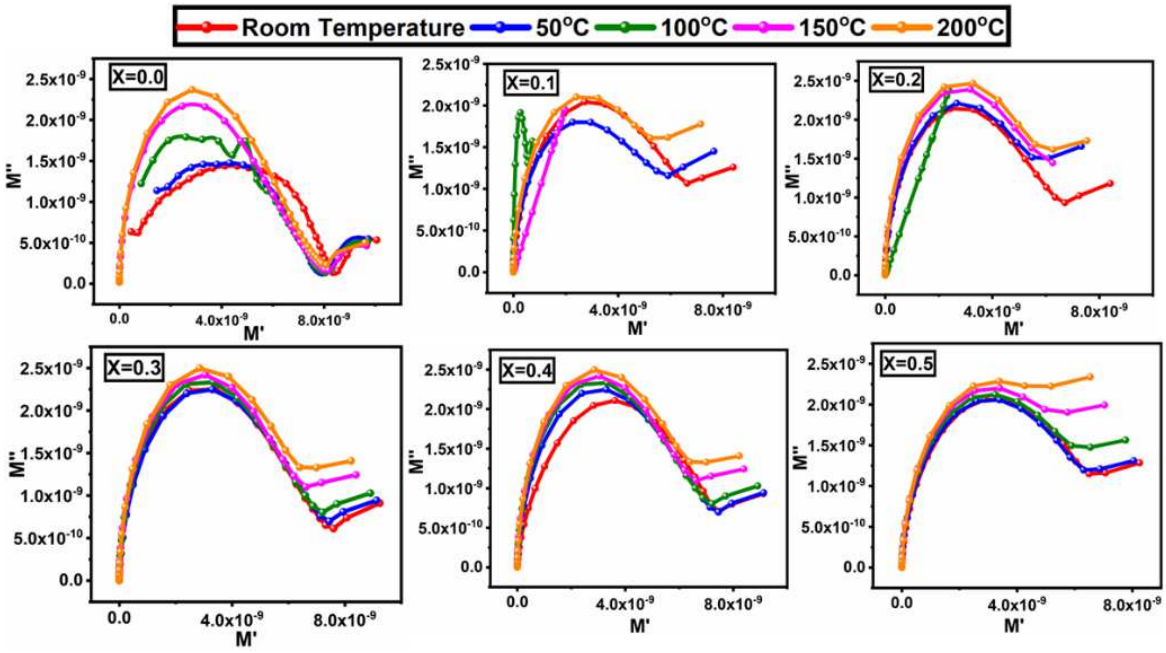


Fig. 13. Complex moduls plane analysis M′ vs M″ for $Co_{0.5}Zn_{0.5-x}Mg_xFe_2O_4$ (x =0.0–0.5) ceramics.

3.5.6. AC conductivity analysis

Fig. 14 presents the frequency dependent AC conductivity (σ_{ac}) of $Co_{0.5}Zn_{0.5-x}Mg_xFe_2O_4$ (x = 0.0–0.5) ferrite ceramics measured over a range of temperatures. The AC conductivity analysis provides valuable information regarding the charge carrier dynamics and the electrical transport mechanism under an alternating electric field. The AC conductivity was calculated using the following relation:

$$\sigma_{ac} = \omega \varepsilon_0 \varepsilon_r tan\delta \qquad (17)$$

where ε_0 is the permittivity of free space (8.854×10^{-12} F m^{-1}), ε_r is the relative permittivity of the material, $\tan\delta$ is the dielectric loss tangent, f is the applied frequency, and $\omega = 2\pi f$ is the angular frequency. The AC conductivity spectra were further analyzed using Jonscher's universal power law:

$$\sigma_{ac}(\omega) = \sigma_{dc} + A\omega^s \quad (18)$$

where σ_{dc} is the DC conductivity, A is a temperature-dependent pre-exponential constant, and s is the frequency exponent. The fitted values of σ_{dc}, A, and s for all compositions at different temperatures are summarized in Table 7. The parameter σ_{dc} represents the long-range migration of charge carriers, whereas A and s describe the frequency-dependent contribution associated with localized hopping conduction. The frequency exponent s remains below unity for all compositions over the investigated temperature range, indicating that the electrical transport is governed by hopping of localized charge carriers. Furthermore, both $\sigma_{dc}$and A increase with increasing Mg concentration, demonstrating the enhancement of charge carrier transport through cation redistribution within the spinel lattice. As shown in Fig. 14, the AC conductivity remains nearly constant in the low-frequency region for all compositions and temperatures, forming a frequency-independent plateau corresponding to the DC conductivity. In this region, charge carrier motion is strongly influenced by grain-boundary resistance and interfacial polarization. With increasing frequency, the AC conductivity increases rapidly owing to the enhanced hopping of localized charge carriers. At higher frequencies, electrons acquire sufficient energy to hop between Fe^{2+} and Fe^{3+} ions occupying the octahedral (B) sites of the spinel lattice, resulting in enhanced electrical conduction. This behavior is consistent with the small polaron hopping mechanism commonly observed in spinel ferrites.

The electrical transport behavior is strongly influenced by Mg substitution. As the Mg concentration increases, the AC conductivity gradually increases over the entire frequency range because of the redistribution of cations and the corresponding increase in the concentration of Fe^{2+}/Fe^{3+} hopping pairs. The substitution of Mg^{2+} modifies the local electronic environment and enhances the hopping probability of charge carriers, thereby improving electrical conductivity. Moreover, the conductivity increases systematically with temperature for all compositions, confirming the thermally activated nature of the conduction process. The observed decrease in the frequency exponent (s) (Table 7) with increasing temperature is consistent with the Correlated Barrier Hopping (CBH) model, indicating that charge transport occurs through thermally activated hopping of localized charge carriers over potential barriers. Therefore, the combined effects of temperature and Mg substitution significantly enhance the electrical transport characteristics of $Co_{0.5}Zn_{0.5-x}Mg_xFe_2O_4$ ferrite ceramics. Similar AC conductivity behavior governed by the CBH mechanism has been reported for related spinel ferrite systems, supporting the present observations [31].

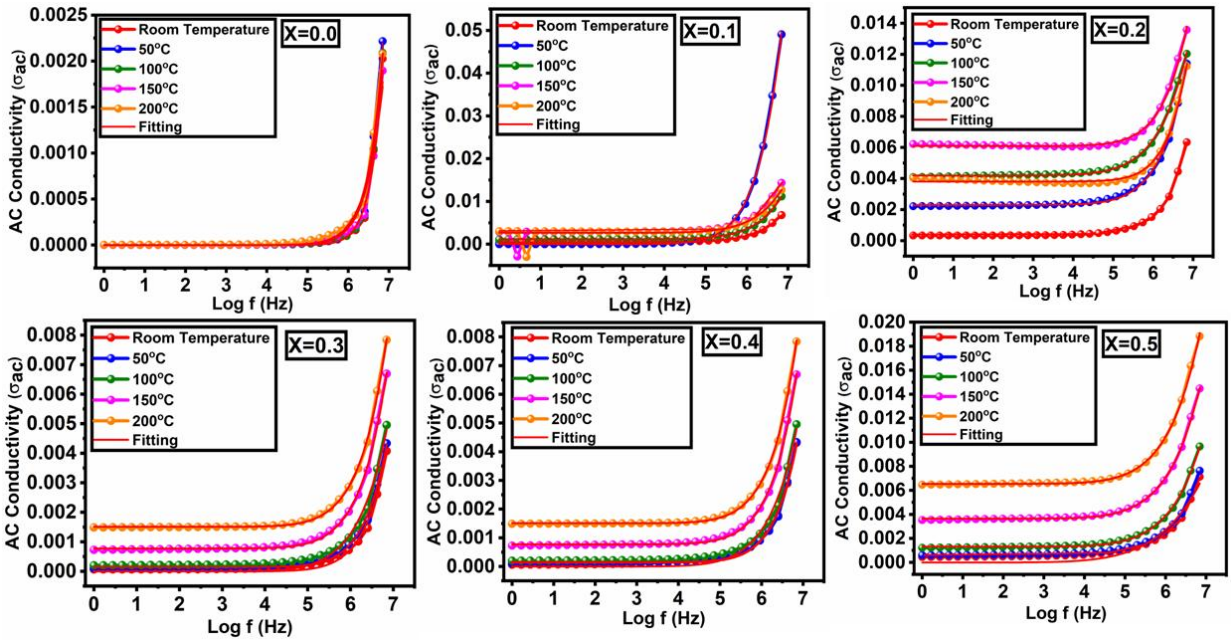


Fig. 14. Dependence of AC conductivity on frequency of $Co_{0.5}Zn_{0.5-x}Mg_xFe_2O_4$ (x =0.0–0.5) ceramics.

Table 7

Jonscher's power-law fitting parameters for $Co_{0.5}Zn_{0.5-x}Mg_xFe_2O_4$ (x =0.0–0.5).

Samples	parameters	RT°C	50°C	100°C	150°C	200°C
X=0.0	σ_{dc}	8.6×10^{-6}	2.1×10^{-5}	2.13×10^{-5}	1.16×10^{-5}	5.06×10^{-5}
	A	6.5×10^{-7}	1.1×10^{-6}	2.2×10^{-6}	3.0×10^{-6}	4.2×10^{-6}
	S	0.93	0.90	0.87	0.84	0.81
X=0.1	σ_{dc}	2.67×10^{-3}	3.95×10^{-4}	1.19×10^{-3}	2.0×10^{-3}	3.0×10^{-3}
	A	4.1×10^{-5}	1.8×10^{-5}	2.9×10^{-5}	3.7×10^{-5}	4.6×10^{-5}
	S	0.79	0.88	0.84	0.80	0.77
X=0.2	σ_{dc}	6.1×10^{-4}	2.3×10^{-3}	4.2×10^{-3}	6.1×10^{-3}	3.81×10^{-3}
	A	8.5×10^{-4}	2.1×10^{-5}	3.8×10^{-5}	5.2×10^{-7}	3.1×10^{-7}
	S	0.92	0.84	0.79	0.74	0.81
X=0.3	σ_{dc}	1.51×10^{-3}	1.44×10^{-4}	7.76×10^{-4}	7.53×10^{-4}	1.10×10^{-4}
	A	1.5×10^{-5}	2.2×10^{-5}	2.6×10^{-5}	3.4×10^{-5}	4.6×10^{-5}
	S	0.91	0.86	0.83	0.80	0.76
X=0.4	σ_{dc}	7.54×10^{-5}	1.4×10^{-4}	1.44×10^{-4}	7.77×10^{-4}	1.51×10^{-3}
	A	4.5×10^{-7}	1.8×10^{-5}	2.3×10^{-5}	3.6×10^{-5}	4.8×10^{-5}
	S	0.94	0.88	0.86	0.81	0.77
X=0.5	σ_{dc}	1.99×10^{-2}	1.32×10^{-3}	1.0×10^{-3}	3.65×10^{-3}	6.55×10^{-3}
	A	3.1×10^{-6}	2.6×10^{-5}	2.1×10^{-5}	3.9×10^{-5}	5.4×10^{-5}
	S	0.95	0.86	0.88	0.82	0.76

3.5.6.1. Activation Energy

The Arrhenius expression given below was used to evaluate the activation energy (E_a) of $Co_{0.5}Zn_{0.5-x}Mg_xFe_2O_4$ (x = 0.1–0.5) ceramics,

$$\sigma_{ac} = \sigma_0 \exp\left(\frac{-E_a}{KT}\right) \qquad (19)$$

Here, k denotes Boltzmann constant and σ_0 denotes pre-exponential factor. The Arrhenius plots for different frequencies of x = 0.1–0.5 ceramics are shown in Fig. 15. The activation energy (E_a) values obtained from the analysis are noted in Table 8 exhibit a reduced with increasing frequencies. At lower frequencies (1 kHz), relatively higher E_a values are observed, suggesting that charge transport is predominantly governed by intergranular resistance. These grain boundaries act as energy barrier requiring higher thermal energy for charge carriers to participate in conduction. The reduction in activation energy that comes with higher frequency, it is tied into more Fe^{2+}/Fe^{3+} hopping happening at the octahedrally coordination. This hopping, it really gets affected when Mg^{2+} is swapped in for Zn^{2+} ions. When those Mg^{2+} ions are put in, they actually change how the cations are spread out inside the spinel structure. So, this changes the amount of Fe^{2+}/Fe^{3+} pairs that are sitting at those octahedrally (B) position. This redistribution allows electron hopping and lowers the energy barrier for conduction. As a result, charge carrier can respond more easily to the AC field and the E_a values are lower at higher frequencies.

The composition part is also has an important part for conduction behaviour. For x=0.1 and 0.3 the higher values of activation energy suggest that the effect of grain boundary is dominating mechanism of conduction. Grain boundaries act as potential barriers, requiring higher thermal energy for carrier migration across them. When x = 0.2, E_a is lower, which suggest charges can move easier. This point to a better path for conduction. For x = 0.4 and x = 0.5, there is a higher E_a at low frequencies, which is caused by lattice distortion and less available hopping sites, Which slows down charge transport. The decrease in activation energy when the frequency and temperature go high supports that this conduction process is thermally activated. Higher temperaturers give enough energy for charges to move more freely and increasing frequency make their dynamic response better. The combined effect reduces the energy requires to start the conduction. Similar low activation energy values have been reported for Co-Zn-Al doped ferrite, indicating hopping-type conduction [54]. Metal oxides used in dielectric studies usually show good dielectric properties with low energy barriers for dipole orientation or charge movement due to their low activation energy. This

response point to the suitability of prepared material for applications in capacitors and high frequency devices.

Table 8

Activation energy from Arrhenius plots of $Co_{0.5}Zn_{0.5-x}Mg_xFe_2O_4$ (x =0.0–0.5).

Frequency (Hz)	Activation Energy					
	x = 0.0	x = 0.1	x = 0.2	x = 0.3	x = 0.4	x = 0.5
1 kHz	0.00301	0.00704	0.00164	0.00757	0.00528	0.00663
10 kHz	0.00254	0.00518	0.00183	0.00659	0.00469	0.00608
1 MHz	0.00145	0.00532	0.00189	0.00316	0.00190	0.00370

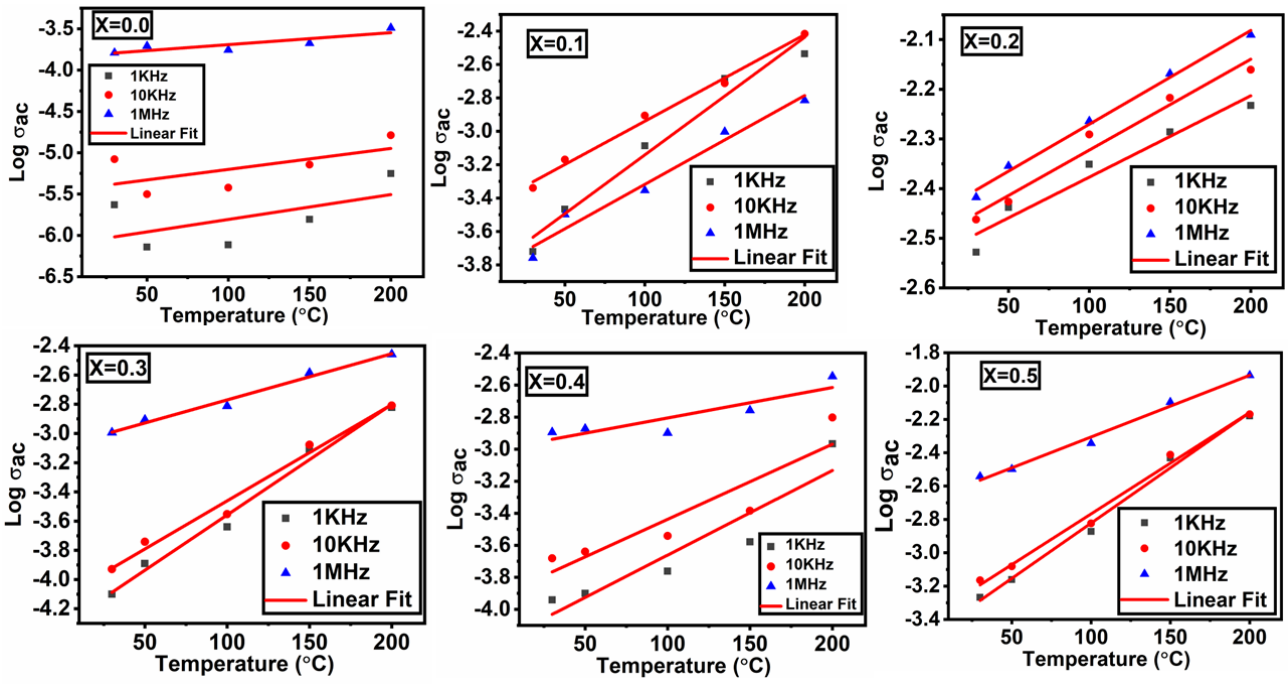


Fig. 15. Arrhenius plots of $Co_{0.5}Zn_{0.5-x}Mg_xFe_2O_4$ (x =0.0–0.5).

3.5.7. Dielectric quality factor (Q)

The frequency dependence of the quality factor (Q) for $Co_{0.5}Zn_{0.5-x}Mg_xFe_2O_4$ (x = 0.1–0.5) ferrite ceramics measured at different temperatures is presented in Fig. S6. The quality factor, defined as $Q = 1/\tan\delta$, is an important parameter for evaluating the dielectric performance of a material, as it represents the ratio of stored energy to energy dissipated during an alternating electric field. Materials with a high quality factor exhibit low dielectric loss and superior energy storage capability, making them attractive for capacitor, high-frequency, and energy storage applications. For all compositions, the quality factor exhibits a strong frequency dependence. At low frequencies, Q remains relatively low because of the large dielectric loss associated with space-charge polarization and the accumulation of charge

carriers at the grain boundaries. In this frequency region, charge carriers and dipoles can effectively follow the applied electric field, resulting in greater energy dissipation. As the frequency increases, the ability of charge carriers and dipoles to respond to the rapidly alternating electric field gradually decreases, leading to a reduction in dielectric loss and a corresponding increase in the quality factor. Consequently, Q increases continuously with frequency and reaches its highest values in the high-frequency region (approximately 10^5–10^7 Hz), where energy dissipation becomes minimal. For some Mg substituted compositions, a broad maximum in the quality factor is observed, which may be associated with dielectric relaxation arising from the hopping of localized charge carriers between Fe^{2+} and Fe^{3+} ions. At higher frequencies, the quality factor becomes nearly stable, indicating a significant reduction in dielectric loss and improved dielectric stability. The enhancement of Q at higher frequencies demonstrates the efficient suppression of energy dissipation and reflects the improved dielectric response of the ferrite ceramics. Similar frequency dependent quality factor behavior has been reported for $Co_{0.2}Ni_{0.5}Zn_{0.3}Eu_xFe_{2-x}O_4$ [55] and $BaZn_{1+x}Mn_xFe_{12-2x}O_{19}$ [56], where the increase in Q was attributed to reduced dielectric loss and enhanced polarization stability at higher frequencies. In summary, the investigated $Co_{0.5}Zn_{0.5-x}Mg_xFe_2O_4$ ferrite ceramics exhibit a high quality factor at elevated frequencies, accompanied by low dielectric loss and controlled energy dissipation. These characteristics demonstrate their potential for high-frequency electronic components, dielectric resonators, capacitors and energy storage devices, where efficient energy storage and minimal dielectric loss are essential.

3.5.8. Bode Plot

The frequency dependence of the phase angle for $Co_{0.5}Zn_{0.5-x}Mg_xFe_2O_4$ (x = 0.0–0.5) ferrite ceramics measured at different temperatures is presented in Fig. 16. The phase angle provides valuable information regarding the electrical relaxation behavior and charge transport mechanism in the investigated ferrite system. At low frequencies, all compositions exhibit phase angles close to 0°, indicating predominantly resistive behavior arising from the significant contribution of grain boundaries and interfacial polarization. As the frequency increases, the phase angle gradually shifts toward more negative values (approximately −80° to −90°), reflecting a transition from resistive to capacitive behavior associated with the dominant response of the grain interiors.

In the intermediate frequency region, a pronounced phase dispersion is observed for all compositions, corresponding to the electrical relaxation process associated with charge carrier polarization. With increasing temperature, this dispersion region shifts progressively toward higher frequencies, indicating faster relaxation dynamics and enhanced mobility of thermally activated charge carriers. The sharper phase transition observed at elevated temperatures suggests an improved polarization response and more efficient charge transport within the ferrite structure. Compared with the undoped composition (x = 0.0), the Mg-substituted samples exhibit a more pronounced frequency-dependent phase transition, indicating enhanced dielectric relaxation and increased hopping probability of charge carriers between Fe^{2+} and Fe^{3+} ions at the octahedral (B) sites. These observations demonstrate that Mg^{2+} substitution effectively improves the electrical response by facilitating thermally activated charge carrier hopping and enhancing the capacitive characteristics of the $Co_{0.5}Zn_{0.5-x}Mg_xFe_2O_4$ ferrite ceramics.

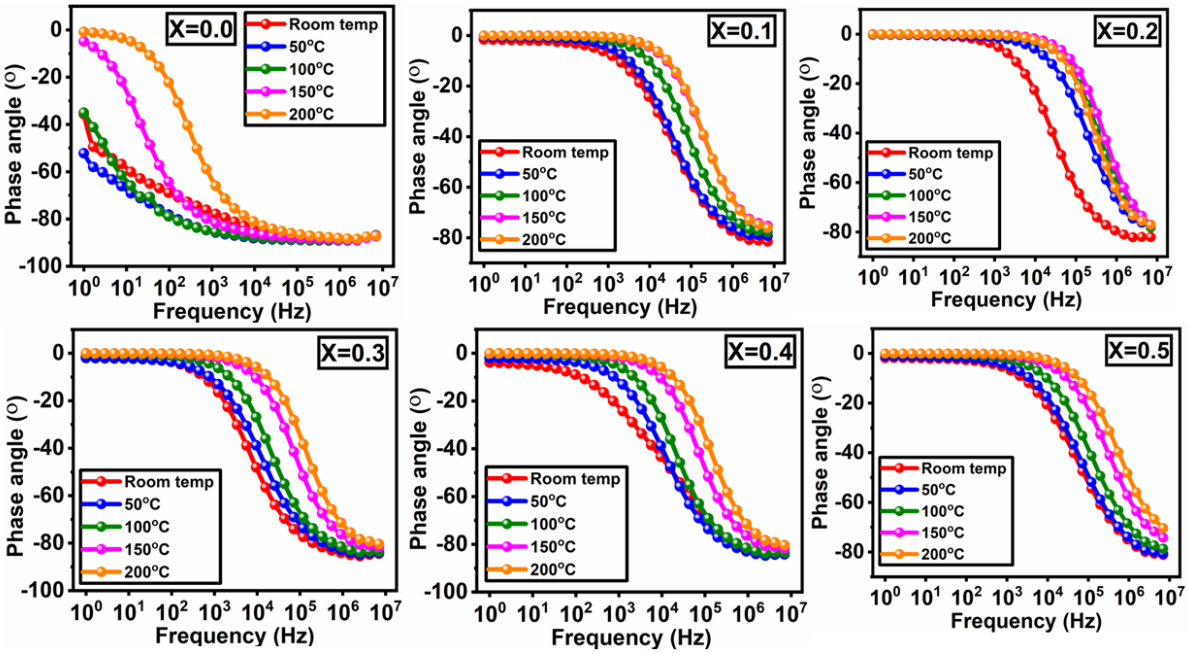


Fig. 16. Frequency dependence of phase angle of $Co_{0.5}Zn_{0.5-x}Mg_xFe_2O_4$ (x =0.0–0.5).

3.5.9. Frequency scaling of normalized impedence

Fig. 17 presents the normalized impedance spectra (Z''/Z''_{max}) as a function of the normalized frequency (f/f_{max}) for $Co_{0.5}Zn_{0.5-x}Mg_xFe_2O_4$ (x = 0.0–0.5) ferrite ceramics measured at different temperatures. Normalization of the imaginary impedance eliminates the influence of its absolute magnitude and facilitates a direct comparison of the relaxation behavior among different compositions and temperatures. The scaling analysis is expressed

as $\frac{Z''}{Z''_{max}} = F\left(\frac{f}{f_{max}}\right)$. where ($f_{max}$) is the frequency corresponding to the maximum value of the imaginary impedance. For an ideal Debye relaxation process, all normalized curves measured at different temperatures are expected to collapse onto a single master curve. Any deviation from this master curve indicates the existence of multiple relaxation processes and a distribution of relaxation times associated with non-Debye behavior.

The normalized impedance spectra of all compositions exhibit broad relaxation peaks with slight deviations from complete overlap, confirming that the electrical relaxation process is predominantly non-Debye in nature. For the undoped sample (x = 0.0), the normalized curves exhibit relatively good overlap, suggesting a comparatively uniform relaxation process. At lower Mg concentrations (x = 0.1 and 0.2), the relaxation peaks remain nearly symmetric with moderate overlap, indicating that the relaxation mechanism is largely temperature independent while still exhibiting a finite distribution of relaxation times. As the Mg concentration increases to x = 0.3 and 0.4, the normalized peaks become broader and slight deviations from the master curve are observed, reflecting the increasing influence of grain-boundary relaxation and microstructural heterogeneity. For the highest Mg concentration (x = 0.5), the broadest relaxation peak and the largest deviation from complete overlap are observed, indicating an increased distribution of relaxation times arising from enhanced carrier localization, lattice disorder, and interfacial polarization.

The gradual broadening of the normalized impedance peaks with increasing Mg substitution demonstrates that Mg^{2+} incorporation progressively modifies the electrical relaxation dynamics by increasing the contribution of grain boundaries to the overall conduction process. The incomplete overlap of the normalized spectra confirms that the relaxation mechanism is governed by multiple thermally activated processes rather than a single Debye relaxation. These observations are consistent with the impedance, modulus, and AC conductivity analyses, which indicate that charge transport occurs predominantly through thermally activated hopping of localized charge carriers. Similar scaling behavior has been reported for $Ni_{0.6-x}Cd_xMg_{0.4}Fe_2O_4$ [57] and $Co_xCu_{1-x}Fe_2O_4$ [58], where deviations from the master curve were attributed to grain-boundary effects and non-Debye relaxation.

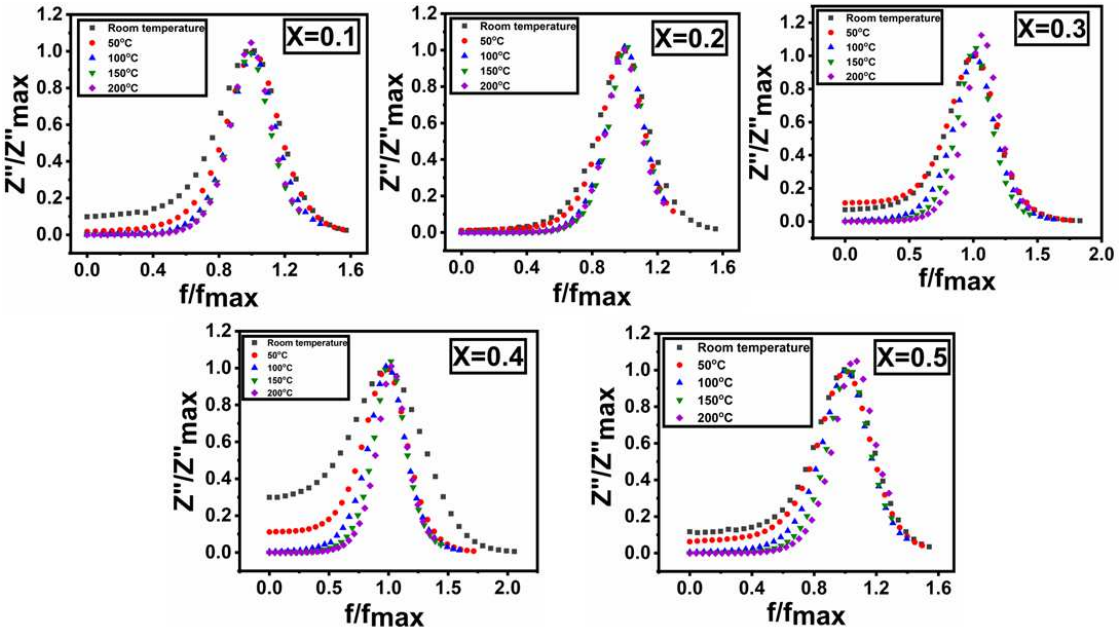


Fig. 17. Plot of normalized impedence $\left(\frac{z''}{z''_{max}}\right)$vs normalized frequency $\left(\frac{f}{f_{max}}\right)$ of $Co_{0.5}Zn_{0.5-x}Mg_xFe_2O_4$ (x =0.0–0.5).

Conclusion

$Co_{0.5}Zn_{0.5-x}Mg_xFe_2O_4$ (x = 0.0–0.5) ceramics were successfully synthesized by the sol–gel method. XRD and Rietveld refinement confirmed the formation of a single-phase cubic spinel structure for all compositions, while FTIR analysis verified the characteristic tetrahedral and octahedral metal–oxygen vibrations, confirming the stability of the spinel framework. Mg substitution significantly modified the optical properties, reducing the band gap and altering the optical parameters (R_L, R_m, and α_m), indicating changes in the electronic structure. Magnetic measurements confirmed ferromagnetic behavior with a multidomain structure ($M_r/M_s < 0.1$), whereas $Co_{0.5}Zn_{0.5}Mg_{0.5}Fe_2O_4$ exhibited soft magnetic characteristics owing to its low coercivity and the highest saturation magnetization among the investigated compositions. Dielectric studies demonstrated that the same composition possessed a high dielectric constant with low dielectric loss. The relaxation times ranged from 10^{-2} to 10^{-7} s. Furthermore, Nyquist plots confirmed the contributions of both grains and grain boundaries to the electrical conduction mechanism. The combined improvements in optical, magnetic, dielectric, and electrical properties demonstrate that Mg substitution effectively tailors the multifunctional performance of Co–Zn ferrites, making $Co_{0.5}Zn_{0.5}Mg_{0.5}Fe_2O_4$ a promising candidate for high-frequency electronic and memory device applications.

Acknowledgments

CRediT authorship contribution statement

B. S. Samyuktha: Writing – original draft, Methodology, Investigation. **A. Sathiya Priya**: Writing – review & editing, Supervision, Methodology, Conceptualization. **D S Jayalakshmi**: Visualization, Validation, Resources, Formal analysis Data curation.

Declaration of competing interest

The authors declare that they have no known competing financial interests or personal relationships that could have appeared to influence the work reported in this paper.

Data and code availability

The data used to support the findings of this study are available from the corresponding authors upon request.

Ethical Approval

This study does not involve human participants or animals, and therefore ethical approval was not required.

Funding

No external funding.

Reference

1. C. ben Makhlouf, M. K. M. Ali, W. Nouira, F. Hcini, W. Chouk, N. B. Hamadi, S. Hcini, M. Gassoumi, Structural, vibrational, and dielectric characterization of sol–gel synthesized spinel ferrite for high-performance multifunctional applications, J Sol-Gel Sci Technol. 118 (2026) 20. https://doi.org/10.1007/s10971-025-07049-0.
2. F. A. Sheikh, Z. A. Gilani, H. M. N. H. K. Asghar, M. Khalid, S. M. Ali, N. -ul-Haq Khan, M. A. Shar, A. K. Khan, Structural, morphological, and magneto-dielectric features of Ni-Co-Pr ferrites for high density memory and high frequency devices, J. Magn. Magn. Mater. 587 (2023) 171240. https://doi.org/10.1016/j.jmmm.2023.171240.
3. Y. Fang, S. Zhang, P. R. Ohodnicki, G. Wang, Relation between cation distribution and chemical bonds in spinel $NiFe_2O_4$, Mater. Today Commun. 33 (2022) 104436. https://doi.org/10.1016/j.mtcomm.2022.104436.
4. K. R. S. -Lievanos, J. L. Stair, K. E. Knowles, Cation Distribution in Spinel Ferrite Nanocrystals: Characterization, Impact on their Physical Properties, and Opportunities

for Synthetic Control, Inorg. Chem. 60 (2021) 4291–4305. https://doi.org/10.1021/acs.inorgchem.1c00040.

5. Md. J. Islam, M. Jhahan, M. T. Khatun, M. N. I. Khan, M. J. Rahman, Md. A. Islam, A. Al-Momin, M. M. Alam, Influence of Mg substitution on structural, magnetic and electrical properties of Zn-Cu ferrites, J Mater Sci: Mater Electron. 32 (2021) 26173–26180. https://doi.org/10.1007/s10854-021-06617-8.
6. M. B. Hossen, A. K. M. A. Hossain, Complex impedance and electric modulus studies of magnetic ceramic $Ni_{0.27}Cu_{0.10}Zn_{0.63}Fe_2O_4$, *J Adv Ceram*. 4 (2015) 217–225. https://doi.org/10.1007/s40145-015-0152-2.
7. R. Yang, X. Yu, H. Li, C. Wang, C. Wu, W. Zhang, W. Guo, Effect of Mg doping on magnetic induction heating of Zn-Co ferrite nanoparticles, J. Alloys Compd. 851 (2021) 156907. https://doi.org/10.1016/j.jallcom.2020.156907.
8. N. I. Abu-Elsaad, A. S. Nawara, Effect of Cu substitution on magnetic and photocatalytic properties of Mn–$ZnFe_2O_4$ nanoparticles, J Mater Sci. 59 (2024) 4167–4185. https://doi.org/10.1007/s10853-024-09486-8.
9. A. S. Priya, D. Geetha, Structural and frequency dependent dielectric properties of Ba doped Ni–Zn ferrite powders, Phosphorus Sulfur Silicon Relat. Elem. 197 (2022) 186–191. https://doi.org/10.1080/10426507.2021.2025375.
10. H. Badiger, B. G. Hegde, S. Kumbar, S. Dodamani, S. Y. Khatavi, S. Matteppanavar, Magnetic, Electric, and Antimicrobial Properties of Chromium- Doped Cobalt Zinc Ferrite Nanoplates, ChemistrySelect, 9 (2024) e202303370. https://doi.org/10.1002/slct.202303370.
11. O. El-Sayed, M. H. Ghozza, R. K. A. El. Hamid, Structure, electrical, and optical properties of $Co_{0.7-x}Zn_xNi_{0.3}Fe_2O_4$ ($0.3 \geq x \geq 0.7$) nano-ferrite by sol–gel auto-combustion technique, J Aust Ceram Soc. 61 (2025) 41–54. https://doi.org/10.1007/s41779-024-01056-0.
12. S. Thammarong, X. Yu, P. Yin, R. Yang, C. Wu, W. Zhang, Synthesis of Ca^{2+} substituted cobalt zinc ferrite nanoparticles for magnetic induction hyperthermia, Mater. Today Commun. 47 (2025) 112975. https://doi.org/10.1016/j.mtcomm.2025.112975.
13. K. E. Rady, A. R. A. El-Salam, E. A. ELFadaly, M. H. Aly, Role of Mn^{2+}ion in the optimization of the structural and dielectric properties of Co–Zn ferrite, Appl. Phys. A. 129 (2023) 245. https://doi.org/10.1007/s00339-023-06528-x.

14. K. Jangam, K. Patil, S. Balgude, S. Patange, P. More, Magnetically separable $Zn_{1-x}Co_{0.5x}Mg_{0.5x}Fe_2O_4$ ferrites: stable and efficient sunlight-driven photocatalyst for environmental remediation, RSC Adv. 10 (2020) 42766. https://doi.org/10.1039/d0ra08172h.
15. D. Chahar, P. Thakur, R. Kumar, A. Thakur, Influence of Mg doping on the structural, electrical and dielectric properties of Co-Zn nanoferrites, J. Magn. Magn. Mater. 544 (2022) 168726. https://doi.org/10.1016/j.jmmm.2021.168726.
16. S. Kumari, F. Wan, A. Thakur, S. Singh, P. Thakur, Retrievable nano-sized Co–Mg–Zn ferrite as an active photocatalyst and adsorbent for removing organic and biological contaminants for water purification, Ceram. Int. 50 (2024) 3210–3221. https://doi.org/10.1016/j.ceramint.2023.11.071.
17. M. N. Akhtar, M. S. Nazir, Z. Tahir, S. Qamar, M. A. Khan, Impact of Co doping on physical, structural, microstructural and magnetic features of MgZn nanoferrites for high frequency applications, Ceram. Int. 46 (2020) 1750-1759. https://doi.org/10.1016/j.ceramint.2019.09.149.
18. H. K. Fadafan, S. Nezhadeini, P. Lotfalinezhad, Thermoelectric Power and Dielectric Studies of Cobalt-Substituted Manganese-Zinc Nanoferrites, J. Supercond. Nov. Magn. 33 (2020) 2037–2042. https://doi.org/10.1007/s10948-020-05459-5.
19. M. Hussain, A. Mehmood, F. Ali, Z. A. Sandhu, M. A. raza, S. Sajid, M. Sohaib, M. T. Khan, A. H. Bhalli, A. Hussain, M. S. Arshid, N. Mehboob, A. G. Al-Sehemi, Tuning the Magnetic Behavior of Zinc Ferrite Via Cobalt Substitution: A Structural Analysis, ACS Omega. 9 (2024) 2536−2546. https://doi.org/10.1021/acsomega.3c07251.
20. M. I. Arshad, M. S. Hasan, A. U. Rehman, N. Amin, L. D. Tung, N.T. K. Thanh, N.A. Morley, M. Amami, F. Alresheedi, S. Ezzine, M.A. Gadhi, Mg-modified Zn-Co-Fe-La nano ferrites: A study of structural, morphological, vibrational, electro-optical, dielectric and magnetic evolution, J. Alloys Compd. 972 (2024) 172847. https://doi.org/10.1016/j.jallcom.2023.172847.
21. M. Beyranvand, A. Gholizadeh, Structural, magnetic, elastic, and dielectric properties of $Mn_{0.3-x}Cd_xCu_{0.2}Zn_{0.5}Fe_2O_4$ nanoparticles, J Mater Sci: Mater Electron. 31 (2020) 5124–5140. https://doi.org/10.1007/s10854-020-03073-8.
22. W. Zhang, A. Sun, X. Pan, Y. Han, X. Zhao, L. Yu, Z. Zuo, N. Suo, Structural, morphological and magnetic properties of Ni–Co ferrites by the Mn^{2+} ions substitution, J. Mater. Sci.: Mater. Electron. 30 (2019) 18729–18743. https://doi.org/10.1007/s10854-019-02226-8.

23. Y. Jiang, A. Sun, X. Huang, J. Wang, Study on the crystal structure and magnetic properties of Zn-Cu-Co nano ferrite doped with Yb^{3+}, J. Alloys Compd. 931 (2023) 167527. https://doi.org/10.1016/j.jallcom.2022.167527.
24. K. K. Bamzai, G. Kour, B. Kaur, S. D. Kulkarni, Preparation, and Structural and Magnetic Properties of Ca Substituted Magnesium Ferrite with Composition $MgCa_xFe_{2-x}O_4$ (x = 0.00, 0.01, 0.03, 0.05, 0.07), J. Mater. (2014) 1-8. https://doi.org/10.1155/2014/184340.
25. A. S. Priya, D. Geetha, N. Kavitha, Effect of Al substitution on the structural, electric and impedance behavior of cobalt ferrite, 160 (2019) 453-460. https://doi.org/10.1016/j.vacuum.2018.12.004.
26. S. J. C. Masuku, J. Z. Msomi, S. Mahule, T. A. Nhlapo, Structural, morphological and electron spin resonance of $Zn_{0.7}Ni_{0.3}Gd_xFe_{2-x}O_4$ ($0 \leq x \leq 0.1$) nanoferrites synthesized via glycol-thermal method, J. Solid State Chem. 349 (2025) 125440. https://doi.org/10.1016/j.jssc.2025.125440.
27. N. I. Abu-Elsaad, R. A. Metwally, A. S. Nawara, Erbium Substituted Mn-Cu Ferrite Nanoparticles: Synthesis, Structural, Magnetic, and Antimicrobial Activity Properties, Braz. J. Phys. 55 (2025) 165. https://doi.org/10.1007/s13538-025-01784-z.
28. S. S. Thomas, I. H. Joe, P. Aswathy, E. Mathew, A. A. Noble, Structural, magnetic, and nonlinear optical properties of calcium doped Ni-Zn ferrite nanoparticles synthesized by co-precipitation method, Mater. Sci. Eng., B. 297 (2023) 116696. https://doi.org/10.1016/j.mseb.2023.116696.
29. K. Ramarao, B. R. Babu, B. K. babu, V. Veeraiah, K. Rajasekhar, B. R. Kumar, B. S. Latha, Enhancement in magnetic and electrical properties of Ni substituted Mg ferrite, Mater. Sci.-Pol. 36 (2018) 644-654, https://doi.org/10.2478/msp-2018-0065.
30. F. Fakhry, E. Shaheen, H. El-Dosoky, T. M. Meaz, M. Mubark, R. El-Shater, Elastic and magnetic characteristics of nano-spinel ferrite $Co_{0.5}$ $Mg_xCu_{0.5-x}Fe_2O_4$, Sci Rep. 14 (2024) 29407. https://doi.org/10.1038/s41598-024-74484-4.
31. P. Saxena, P. Choudhary, A. Yadav, V. N. Rai, M. Varshney, A. Mishra, Effect of transition metal substitution on structural and dielectric properties of $Mg_{0.5}Zn_{0.5-x}Cr_xCo_2O_4$ ($0.0 \leq x \leq 0.5$) cobaltite, J. Mater. Sci.: Mater. Electron. 30 (2019) 7292–7300. https://doi.org/10.1007/s10854-019-01042-4.
32. A. Sahai, N. Goswami, Structural and vibrational properties of ZnO nanoparticles synthesized by chemical precipitation method, Phys. E Low-dimens. Syst. Nanostruct. 58 (2014) 130–137, https://doi.org/10.1016/j.physe.2013.12.009.

33. D. M. Byler, H. Susi, W. C. Damert, Relation between force constant and bond length for carbon—nitrogen bonds, Spectrochim. Acta Mol. Biomol. Spectrosc. 43 (1987) 861–863, https://doi.org/10.1016/0584-8539(87)80231-3.
34. T. Tatarchuk, A. Shyichuk, Z. Sojka, J. Grybos, Mu. Naushad, V. Kotsyubynsky, M. Kowalska, S. K. Marks, N. Danyliuk, Green synthesis, structure, cations distribution and bonding characteristics of superparamagnetic cobalt-zinc ferrites nanoparticles for Pb(II) adsorption and magnetic hyperthermia applications, J. Mol. Liq. 328 (2021) 115375. https://doi.org/10.1016/j.molliq.2021.115375.
35. M. M. Hussein, S. A. Saafan, H. F. Abosheiasha, D. Zhou, M. G. Vakhitov, S. V. Trukhanov, A. V. Trukhanov, D. S. Klygach, T. I. Zubar, K. A. Astapovich, H. M. H. Zakalyhi, M. A. Darwisha, Crystal structure and peculiarities of microwave parameters of $Co_{1-x}Ni_xFe_2O_4$ nano spinel ferrites, RSC Adv. 13 (2023) 26879. https://doi.org/10.1039/d3ra04557a.
36. A. M. Moustafa, S. A. Gad, H. M. Hashem, Mg^{2+} Doped ZCFAO Spinel Ferrite: Structural, Optical, Dielectric and Magnetic Explorations, J Inorg Organomet Polym 34 (2024) 3866–3879. https://doi.org/10.1007/s10904-024-03024-4.
37. M. M. El-Masry, M. M. Arman, Cobalt, nickel and zinc spinel ferrites with high transmittance and UV-blocking for advanced optical applications, Sci Rep. 15 (2025) 16636. https://doi.org/10.1038/s41598-025-99604-6.
38. E. Girgis, M. MS. Wahsh, A. GM. Othman, L. Bandhu, KV. Rao, Synthesis, magnetic and optical properties of core/shell $Co_{1-x}Zn_xFe_2O_4/SiO_2$ nanoparticles, Nanoscale Res Lett. 6 (2011) 460. https://doi.org/10.1186/1556-276X-6-460.
39. P. Chand, S. Vaish, P. Kumar, Structural, optical and dielectric properties of transition metal (MFe2O4; M =Co, Ni and Zn) nanoferrites, Phys. B Condens. Matter. 524 (2017) 53–63, https://doi.org/10.1016/j.physb.2017.08.060.
40. E. Hema, A. Manikandan, P. Karthika, S. A. Antony, B. R. Venkatraman, A Novel Synthesis of Zn^{2+}-Doped $CoFe_2O_4$ Spinel Nanoparticles: Structural, Morphological, Opto-magnetic and Catalytic Properties. J Supercond Nov Magn. 28 (2015) 2539–2552 https://doi.org/10.1007/s10948-015-3054-1.
41. H. Kumari, S. Sharma, A. Kumar, R. Parmar, P. Rani, P. Godara, R. M. Singh, R. Jain, Asha, Structural, magnetic, and photocatalytic properties of Ce^{3+} ion doped Ni–Zn ferrite nanoparticles, J. Magn. Magn. Mater. 636 (2025) 173671. https://doi.org/10.1016/j.jmmm.2025.173671.

42. A. Aftabi, A. Babakhani, R. Khoshlahni, Optimized Zn substituted $CoFe_2O_4$ nanoparticles for high efficiency magnetic hyperthermia in biomedical applications, Sci Rep. 15 (2025) 10039. https://doi.org/10.1038/s41598-025-94535-8.
43. T. R. Tatarchuk, N. D. Paliychuk, M. Bououdina, B. Al-Najar, M. Pacia, W. Macyk, A. Shyichuk, Effect of cobalt substitution on structural, elastic, magnetic and optical properties of zinc ferrite nanoparticles, J. Alloys Compd. 731 (2018) 1256-1266. https://doi.org/10.1016/j.jallcom.2017.10.103.
44. X. Liu, B. Zhou, B. Yuan, Z. Liu, Dependences of Magnetic Properties on the Grain Size and Hard/Soft Magnetic Phase Volume Ratio for $Ce_2Fe_{14}B$/α-Fe and $Nd_2Fe_{14}B$/α-Fe Nanocomposites, Materials, 16 (2023) 5260. https://doi.org/10.3390/ma16155260.
45. S. Gautam, R. Charak, S. Garg, P. K. Thakur, N. Goyal, K. H. Chae, Y. Kim, Tailoring magnetism in chromium-doped zinc cobalt ferrite nanostructure for advanced spintronic memory devices, Mater. Today Chem. 41 (2024) 102291. https://doi.org/10.1016/j.mtchem.2024.102291.
46. A. Lahrichi, Y. E. Issmaeli, E. E. N. Madila, S. Rousselot, M. Dolle, M. Slaoui, F. Abdi, T. Lamcharfi, A. Duong , Tuning dielectric performance in novel $Na_{1/2}Er_{1/2}Cu_3Ti_4O_{12}$ ceramics: The interplay of sintering temperature, grain size, and grain boundary resistance, Mater. Chem. Phys. 318 (2024) 129237. https://doi.org/10.1016/j.matchemphys.2024.129237.
47. S. B. Amor, A. Benali, M. Bejar, E. Dhahri, K. Khirouni, M. A. Valente, M. P. F. Graça, F. Al-Turjman, J. Rodriguez, A. Radwan, Modulation of magnetism and study of impedance and alternating current conductivity of $Zn_{0.4}Ni_{0.6}Fe_2O_4$ spinel ferrite, J. Mol. Struct. 1184 (2019) 298e304. https://doi.org/10.1016/j.molstruc.2019.02.053.
48. S. Minz, S. C. Sahoo, S. K. Rout, M. Kar, B. Behera, Structural, magnetic, impedance and electric modulus response and dielectric relaxation in Co-doped inverse spinel $CuFe_2O_4$ nanoferrite, Chem. Phys. Impact. 8 (2024) 100592. https://doi.org/10.1016/j.chphi.2024.100592.
49. M. F. Mahmood, M. B. Hossen, Dynamics of complex impedance, dielectric and electric modulus for NiCuZn ferrites with theoretical justification, Int. Nano Lett.12 (2022), https://doi.org/10.1007/s40089-021-00363-9.
50. A. Zaman, A. Ali, H. Shahid, S. H. Alrefaee, S. Knani, V. Tirth, A. Algahtani, N. Elboughdiri, Study on the structural, optical, vibrational and dielectric properties of Cr^{2+}-doped $SnFe_2O_4$ spinel ferrites, RSC Adv. 15 (2025) 37050-37061. https://doi.org/10.1039/D5RA05190H.

51. I. Soudani, K. B. Brahim, A. Oueslati, A. Aydi, K. Khirouni, A. Benali, E. Dhahri, M. A. Valente, Research on the physical properties of $LiMn_{0.5}Fe_2O_4$ spinel ferrites by the combination of optical, magnetic, and dielectric behaviors, *RSC Adv.* 13 (2023) 9260-9272. https://doi.org/10.1039/D3RA00985H.
52. M. Z. Ahsan, M. M. Kamal, S. S. Rakhi, S. N. Tanha, G. I. Hasan, Electric modulus of manganese doped cobalt ferrite nanoparticles, Results Phys. 50 (2023) 106593. https://doi.org/10.1016/j.rinp.2023.106593.
53. R. Ranjan, R. Kumar, N. Kumar, B. Behera, R. N. P. Choudhary, Impedance and electric modulus analysis of Sm-modified Pb $(Zr_{0.55}Ti_{0.45})_{1-x/4}O_3$, J. Alloys Compd. 509 (2011) 6388–6394. https://doi.org/10.1016/j.jallcom.2011.03.003.
54. S. Singhal, R. Sharma, T. Namgyal, S. Jauhar, S. Bhukal, J. Kaur, Structural, electrical and magnetic properties of Co0.5Zn0.5AlxFe2 xO4 (x = 0, 0.2, 0.4, 0.6, 0.8 and 1.0) prepared via sol–gel route, Ceram. Int. 38 (2012) 2773–2778. https://doi.org/10.1016/j.ceramint.2011.11.047.
55. M. S. Sikder, M. D. Hossain, I. Sardar, Md. S. Hossain, M. N. I. Khan, M. R. Rahman, Improved magnetic and dielectric quality factors with low losses in rare earth (Eu) substituted Co-Ni-Zn ferrites for high frequency devices, Results Phys. 46 (2023) 106320. https://doi.org/10.1016/j.rinp.2023.106320.
56. S. H. Khoreem, A. A. M. Othman, A. H. AL-Hammadi, Enhancing dielectric permittivity in barium ferrite: a novel material for energy storage and advanced electronics applications. Discov Appl Sci. 7 (2025) 322. https://doi.org/10.1007/s42452-025-06801-z.
57. M. B. H. Hamida, T. Mzoughi, N. Hamdaoui, Improvement of Magnetic and Dielectric Properties Through Cd Substitution in Mg–Ni Spinel Ferrite. J Inorg Organomet Polym. 34 (2024) 3848–3865. https://doi.org/10.1007/s10904-024-03061-z.
58. E. H. El-Ghazzawy, S. A. Saafan, N. M. Abo-aita, M. A. Eid, A. S. Atlam, Enhanced physical properties and antimicrobial activity of PEG-4000 capping on $Co_xCu_{1-x}Fe_2O_4$ nanoparticles for technological applications: Synthesis and characterization. J Sol-Gel Sci Technol. 116 (2025) 1797–1820. https://doi.org/10.1007/s10971-025-06974-4.

Supplementary Files

This is a list of supplementary files associated with this preprint. Click to download.

- supplementaryfile1.docx